

Relation of Observable Stellar Parameters to Mass-Loss Rate of AGB Stars in the LMC

HENRY A. PRAGER ^{1,2}, LEE ANNE WILLSON ³, MASSIMO MARENGO ³ AND MICHELLE J. CREECH-EAKMAN ¹

¹*New Mexico Institute of Mining and Technology*

Department of Physics

801 Leroy Place

Socorro, NM 87801, USA

²*Los Alamos National Laboratory*

Los Alamos, NM 87545

³*Iowa State University*

Department of Physics and Astronomy

2323 Osborn Drive

Ames, IA 50011, USA

ABSTRACT

Using the Riebel et al. (2012) data set for 6,889 pulsating AGB stars in the LMC, we have derived formulae for mass-loss rate as a function of luminosity and pulsation period or luminosity and mass in three ways, for each of five subsets of data: fundamental mode oxygen rich stars, first overtone mode oxygen rich stars, fundamental mode carbon stars, first overtone mode carbon stars, and extreme carbon stars. Using the distribution of the stars in period versus luminosity and mass versus luminosity, we are able to derive a power-law fit to the dependence of mass-loss rate on those quantities. This results in formulae that reproduce observed mass-loss rates and are in general agreement with the expectation from mass-loss models that the mass-loss rate is highly sensitive to luminosity, mass, and pulsation period.

In the process of carrying out this analysis we have found radius-mass-luminosity and examined pulsation-mass-radius relations using published evolutionary and pulsation models. These allow us to derive mass and radius from the observed quantities luminosity and pulsation period. We also derived new mass-loss rate versus color relations.

Keywords: Asymptotic giant branch (108), Carbon stars (199), Evolved stars (481), Extreme carbon stars (512), Giant stars (655), Large Magellanic Cloud (903), Late-type giant stars (908), M giant stars (983), M stars (985), Mira variable stars (1066), Pulsating variable stars (1307), Pulsation modes (1309), Semi-regular variable stars (1444), Stellar mass loss (1613), Stellar pulsations (1625), SRa variable stars (2010), Low mass stars (2050), Asymptotic giant branch stars (2100)

1. INTRODUCTION

Asymptotic giant branch (AGB) stars have inert carbon/oxygen cores with concentric hydrogen and helium-burning shells, surrounded by an expanded stellar envelope (see Herwig (2005) and references therein). Near the tip of the AGB, hydrogen and helium burning alternate in thermal pulses, also called helium shell flashes; this produces modulation in the luminosity of the stars over 10,000 to 100,000 year cycles. Near the tip of the AGB the stars become unstable to pulsation, becoming Mira or semi-regular variables with large variations in visual magnitude, radius, and luminosity with pulsation periods of hundreds of days. The pulsation, combined with the formation of dust, drives a high mass-loss rate, removing most of the envelope in a mere 200,000 years (Willson 2000). When the envelope mass gets small enough, the star shrinks as it removes the residual envelope material, and what was the core becomes a new white dwarf star. Mass loss near the tip of the AGB is a major source of interstellar dust, and it is the mechanism by which stellar material, enriched with *s*-process elements and carbon, returns to the interstellar medium (see reviews by Willson (2000) and Höfner & Olofsson (2018) for greater detail).

The first widely used mass loss formula for AGB stars was derived by Reimers (1975) from a small sample of red giants and supergiants, including a few AGB stars. As more data on M giant stars (on the red giant branch–RGB–and the asymptotic giant branch) became available, it was evident that this formula over predicted the mass-loss rates of RGB stars and under predicted the mass-loss rates in AGB stars, especially at the end of their lifetimes (Kudritzki & Reimers 1978). A number of other formulae were proposed based on observations or modeling of the mass loss process: Baud & Habing (1983); Volk & Kwok (1988); Bryan et al. (1990); Blöcker (1995); van Loon et al. (2005); Wachter et al. (2002); Schröder & Cuntz (2005). A similar small-exponent dependence on parameters was found also by Srinivasan et al. (2009) and Goldman et al. (2017), but as Riebel et al. (2012) note the scatter in this data is so large that luminosity dependence cannot be estimated using standard methods. Alternative approaches have been taken by Vassiliadis & Wood (1993) and De Beck et al. (2010), fitting the mass-loss rate as an exponential function of period alone, yielding significantly better fits to model data than the Reimers-like formulas. Vassiliadis & Wood (1993)’s exponential formula produces a much steeper dependence on stellar parameters; steeper dependence is also supported by Kamath et al. (2010), based on models of stellar clusters that needed steeper mass-loss dependence to match their observed evolutionary histories, and by Danilovich et al. (2015), who found $\dot{M} \propto L_*^5$.

Models for this mass-loss process are challenging because it is characterized by feedback between dynamics and grain growth in a low-density atmosphere that cannot be treated with equilibrium physics (Bowen 1988; Willson 2000; Höfner & Olofsson 2018). Several different mass-loss modeling codes are in use, each making different approximations or assumptions about the details. Overall, the results are similar: neither pulsation nor dust alone are capable of producing the high mass-loss rates that are observed, but they can do so when treated together (Willson 2000; Höfner & Olofsson 2018). In one dimension, the most detailed physical models are based on the DARWIN code (Höfner et al. 2003, 2016). These models continue to become more sophisticated, such as through incorporating aluminum oxides and gradual iron enrichment (Höfner et al. 2016, 2022). However, significant gaps in our understanding of mass loss remain, including applicability in low metallicity stars on the AGB (McDonald et al. 2018) to the far more massive red supergiant stars (Beasor & Smith 2022). Most models also do not yet incorporate a full range of known physical effects such as dust-gas drift, departure from local thermodynamic and/or chemical equilibrium, or purely multi-dimensional processes such as convection (Höfner & Olofsson 2018).

The primary goal of this work is to constrain the exponents (B , C) for a power-law approximation $\dot{M} = AL^B M^C$ for a large, homogeneous sample of stars in the LMC, using a subset of the data set by Riebel et al. (2012), with the selection process described in Section 3. This addresses the discrepancy in luminosity dependence of mass-loss rates as measured by CO lines and as measured using dust, as noted in Höfner & Olofsson (2018). We also derive limits on the lead coefficient A , which determines at what luminosity this pattern appears. A is sensitive to some parameters that are less certain, but can be determined to be within a narrow range from the observations.

To examine the evolutionary behavior and compare with previous mass loss formulae we also needed to derive masses and radii. To do this we use evolutionary tracks to get the radius R as a function of luminosity L and mass M (see Section 4.1), and pulsation studies to get the pulsation period P as a function of M and R (see Section 4.2).

2. METHODOLOGY

We define the critical mass-loss rate $\dot{M} = M/t_{\text{ev}}$

$$\frac{1}{t_{\text{ev}}} \equiv \frac{1}{L} \frac{dL}{dt} = \frac{d \ln L}{dt}. \quad (1)$$

To derive t_{ev} , we look at the core mass–luminosity relations. These relations are discussed by Boothroyd & Sackmann (1988), who summarize prior work, and more recently by Trabucchi et al. (2019). For a relation of the form $L = C_1(M_c - C_2)$, where L is the luminosity and M_c is the core mass, we have $dL/dt = C_1 dM_c/dt$ and an energy conversion rate $L = 0.006c^2 dM_c/dt$ (where c is the speed of light) (Kippenhahn et al. 2013), giving

$$t_{\text{ev}} = \frac{8.84 \times 10^{10}}{C_1} \text{ yr} \quad (2)$$

with C_1 in solar units. The relations summarized in the above cited papers tell us t_{ev} is between 1.3 and 1.6 Myr, with a hint that lower metallicity stars will have slower evolution. We conclude that t_{ev} is likely between 1.2 and 1.7 Myr for the LMC stars. We have chosen to set $\log(1/t_{\text{ev}}) = \log(\dot{M}_{\text{crit.}}/M) = -6.2$, equivalent to $t_{\text{ev}} = 10^{6.2} \text{ yr} \approx 1.58 \text{ Myr}$. Note that the evolution time is not the same as the AGB lifetime. It is a characteristic time that describes the growth

of luminosity over the lifetime of the star. From t_{ev} , we can define the critical mass-loss rate, or the death line, where luminosity-dominated evolution shifts to mass-dominated evolution.

$$\left(\frac{1}{M} \frac{dM}{dt}\right)_{\text{crit.}} = \frac{\dot{M}_{\text{crit.}}}{M} = \frac{1}{L} \frac{dL}{dt} = \frac{1}{t_{\text{ev}}} \quad (3)$$

In earlier work (*e.g.*, Bowen & Willson 1991), the death line was sometimes referred to as “the (AGB) cliff”. This will be further discussed and used in Section 5.2.

We have examined two independent methods for constraining the exponents: (a) bilinear fits to the mass-loss rate, luminosity, and pulsation period (see Section 5.1) and (b) fitting the slope and width of the distribution and mass-losses of stars in luminosity–pulsation period space (see Section 5.2). We will see that direct linear fits using \dot{M} result in low reliability as we move further from the mean mass-loss rate, fits with L as the dependent variable are unreliable due to high scatter in that parameter, and that formulas found using the PL strip result in the overall best fits with similar reliability throughout the range of mass-loss rates while having tolerable amounts of spread. Finally, we will examine these results in the context of prior mass-loss formulae and the limitations imposed by observation and the methods used (see Section 6). In the process of this work, we have also determined new mass-loss rate–color relations, and these can be found in Appendix A.

The primary limitation of this study is that it has only been done for one metallicity, assumed appropriate for all of the LMC stars. We have also only considered two bins of C/O , while the mass-loss rates may be sensitive to the values within each bin.

We have used a fixed dust-to-gas ratio to translate observed dust mass-loss rates to total mass-loss rates, based on estimates from the literature. If our value is incorrect but there is a single value that works for all mass-loss rates, the effect will be to shift the pattern without changing the derived exponents. However, the dust-to-gas ratio is potentially sensitive both to C/O and to the mass-loss rate; this could affect the exponents in the mass-loss formula. There is also the potential for a mass-loss dependent bias due to fixed expansion velocities (McDonald et al. 2018).

3. PHOTOMETRIC CATALOG

For this analysis, we are using the data compiled in Riebel et al. (2010) and Riebel et al. (2012); the authors have fitted models from the “Grid of Red Supergiant and Asymptotic Giant Branch Models (GRAMS)” (Sargent et al. 2011; Srinivasan et al. 2011) to all known AGB and red supergiant (RSG) stars in the Large Magellanic Cloud, combining results from the photometric Magellanic Clouds Photometric Survey (MCPS) (Zaritsky et al. 2004), Two Micron All Sky Survey (2MASS) survey (Skrutskie et al. 2006), and Surveying the Agents of a Galaxy’s Evolution (SAGE) (Meixner et al. 2006) survey with the variability data from the MAssive Compact Halo Objects (MACHO) survey (Alcock et al. 1997) which have been refitted by Fraser et al. (2008). Because the Riebel et al. (2012) data set includes RSG, AGB, and other long-period variable stars, we sorted out the AGB stars from the rest of the data set. We can distinguish AGB stars from the others based on their brightness, pulsation periods, and colors.

We are particularly interested in the behavior of stars that are near the death line (defined in Section 1). The evolution time $1/t_{\text{ev}} = L^{-1}dL/dt = d \ln L/dt$ is constant for a star on the AGB with a core mass-luminosity relation as posited in Section 2, such that $\Delta \log L \approx 2.3\Delta t/t_{\text{ev}}$. The death line or cliff is defined by where $\dot{M} = \dot{M}_{\text{crit.}} = M/t_{\text{ev}}$, and can be demonstrated in either $M(t)$ or $\log M$ vs. $\log L$. The region around the death line ($0.1\dot{M}_{\text{crit.}} < \dot{M} < 10\dot{M}_{\text{crit.}}$) is the “death zone”. The death zone is where AGB stars shift from luminosity-dominated evolution to mass-dominated evolution. Thus, this analysis does not attempt to include stars with the very highest mass-loss rates ($\dot{M} \gtrsim 2 \times 10^{-5} M_{\odot}/\text{yr}$) or the longest periods (the longest period in the selected set is 817.7 days), where the models show that the physics of the mass loss process may fundamentally change (Willson 2000; Höfner & Olofsson 2018).

The GRAMS dust mass-loss rates have some limitations. As described in detail in Riebel et al. (2012), the grid assumes spherical symmetry, fixed expansion velocities, dust compositions, and optical constants. These assumptions may lead to systematic errors in the mass-loss rates. Of particular note, the effects of optical constants are particularly strong in the carbon stars (Groenewegen & Sloan 2018) and the fixed expansion velocities potentially cause a mass-loss dependent bias (McDonald et al. 2018). However, this data set is exceptional in its size, being an order of magnitude larger than what we have for local AGB stars, making it ideal for the population-scale analysis seen in Section 5.2.

We are most interested in AGB stars pulsating in the fundamental and first overtone modes. In a period-magnitude diagram, these stars are found in sequences 1 and 2, as defined by Riebel et al. (2010) and following previous works: Wood et al. (1999); Ita et al. (2004); Fraser et al. (2005); and Glass et al. (2009). To efficiently pick stars in these

sequences out, we defined them in log-log space using $3.6 \mu\text{m}$ flux, converted to magnitude using the photometric zero point of $F = 280.9 \text{ Jy}$ (Fazio et al. 2004), and pulsation period (P) to define linear bounds.

$$\text{Seq. 1, Right: } [3.6] = 6.97(\log P - 2.51) + 9.25 \quad (4)$$

$$\text{Seq. 1, Left: } [3.6] = 3.68(\log P - 2.73) + 9.44 \quad (5)$$

$$\text{Seq. 2, Right: } [3.6] = 5.21(\log P - 2.57) + 8.42 \quad (6)$$

$$\text{Seq. 2, Left: } [3.6] = \begin{cases} 4.56(\log P - 2.12) + 10.04 & \text{if } P \leq 120 \\ 6.39(\log P - 2.30) + 8.81 & \text{if } P > 120 \end{cases} \quad (7)$$

These bounds and the stars found within are depicted in Figure 1. RSGs are also present in this data set, so to limit their presence as much as possible, we cut all M stars brighter than $[3.6] = 10.3 \text{ mag}$ and $\log L > 4.5$. The stars with relative errors > 1 , or no reported error in \dot{M} or L , have been removed as well. We have also removed stars with a derived mass $M < 0.45 M_{\odot}$ —below the lowest final mass predicted by initial-final mass relations (Kalirai et al. 2014; Zhao et al. 2012). These masses were derived using the relations established in Section 4.

AGB stars can be divided into two types based on the ratio of carbon to oxygen: $C/O < 1$ (M stars) and $C/O > 1$ (carbon – C – stars). In the LMC, the stars can be distinguished by color and magnitude (see Blum et al. (2006) for details), and have already been separated as such in the Riebel et al. (2012) data set. We have continued to use this classification here. Further, the carbon stars pulsating in the fundamental-mode undergo an extreme mass-loss phase, so they can be split into “normal” AGB stars and “extreme” (xAGB) stars. To separate the two populations, we followed the procedures found in Blum et al. (2006); Srinivasan et al. (2009); and Boyer et al. (2011), among others. In these papers, xAGB stars are defined as fundamental mode carbon stars brighter than the $3.6 \mu\text{m}$ tip of the red giant branch (TRGB) and with $J - [3.6] > 3.1 \text{ mag}$, with a fallback classification of $[3.6] - [8] > 0.8$ for stars brighter than the $3.6 \mu\text{m}$ TRGB with no near-infrared observations. In the Riebel et al. (2012) data set, nearly all carbon stars have measurements in the J band and in the $3.6 \mu\text{m}$ band, and are thus classified using those measurements (Figure 2). The final results of the classification of stars based on sequence and C/O composition can be found in Table 1, along with the mean standard deviation of the mass-loss rates in the final column.

Table 1. Statistics of Analyzed AGB Stars

C/O Ratio	Pulsation Mode	Notes	Identifier	Count	Min., Median, Max. ($\log \dot{M}$)	$\sigma_{\log \dot{M}}$
< 1	Fundamental		M0	1979	-7.83, -6.42, -5.14	0.39
< 1	First Overtone		M1	2162	-7.97, -6.57, -4.96	0.44
> 1	Fundamental		C0	1654	-7.67, -6.62, -5.44	0.25
> 1	Fundamental	Extreme AGB	C0x	341	-6.49, -5.74, -4.67	0.34
> 1	First Overtone		C1	781	-7.68, -6.56, -4.33	0.29

NOTE—Properties and identifiers for our five AGB star categories. As we will see in Section 5, the C0x population is a continuation of the C0 population.

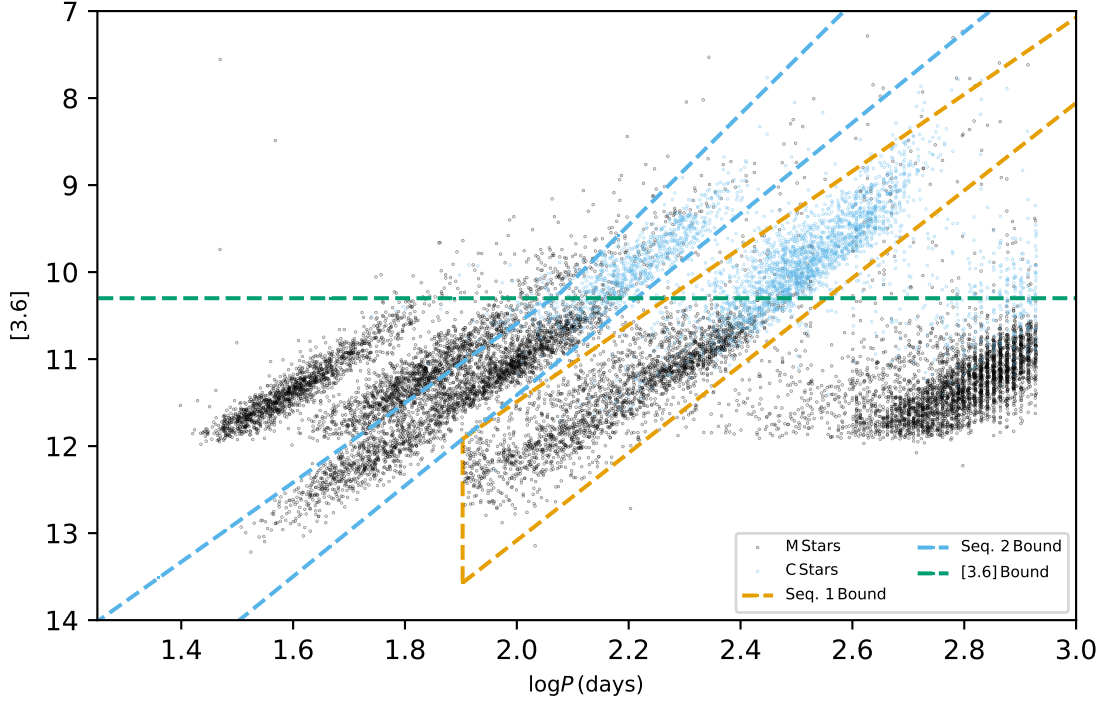


Figure 1. Plot of $[3.6]$ vs $\log P$ for the stars in the Riebel et al. (2012) data set. M-type stars are in black and C-type stars in blue. M stars brighter than $[3.6] = 10.3$ are assumed to be red supergiant stars, and are excluded from the analysis. Following the naming convention established in Riebel et al. (2010), sequence 1 defines AGB stars pulsating in the fundamental-mode, and sequence 2 defines AGB stars pulsating in the first overtone-mode. Definitions of the sequence bounds can be found in equations 4–7.

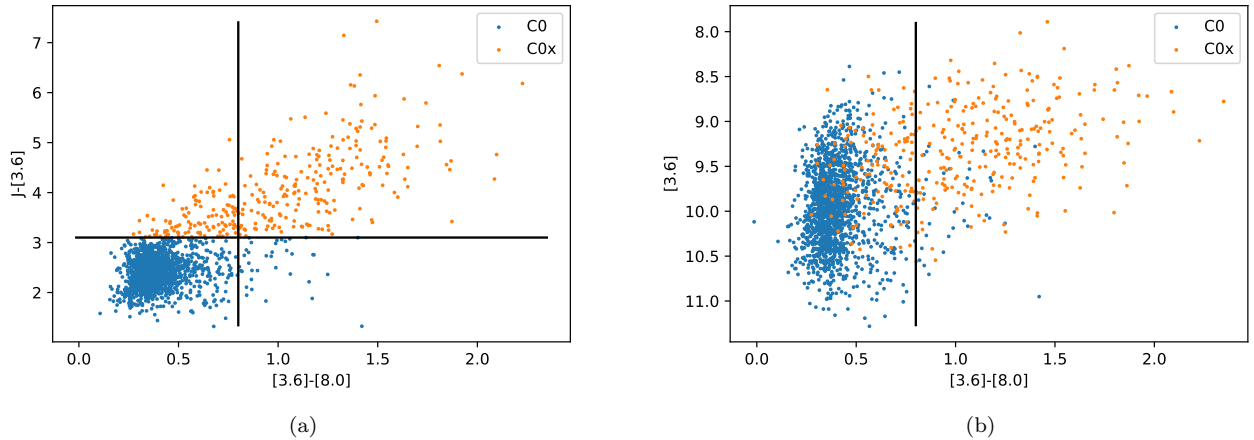


Figure 2. The split of carbon-rich, fundamental-mode pulsator (C0) AGB stars into ‘normal’ and ‘extreme’ populations is depicted here, using the method found in Blum et al. (2006); Srinivasan et al. (2009); and Boyer et al. (2011), where xAGB stars are those brighter than the $3.6 \mu\text{m}$ TRGB and with $J - [3.6] > 3.1$ mag (a), or if there is no near-IR detection, $[3.6] - [8.0] > 0.8$ (b). Stars in blue are ‘normal’ C-stars, and stars in orange are ‘extreme’ AGB stars. All stars were able to be sorted through the primary method, so the scattered blue stars in figure (b) may be ignored.

The pulsation period P is well established, but the luminosity L is subject to significant scatter. This scatter limits our ability to narrow the dependence of \dot{M} on L using these observations (Riebel et al. 2012; Höfner & Olofsson 2018), and we will see this appearing as regression dilution (Spearman 1904; Frost & Thompson 2000; Carroll et al. 2006) in the fits. To get around this issue, we will explore two complementary methods for constraining the mass-loss formulae using this data, in Sections 5.1 and 5.2. When the color is taken into account, there is an observational distinction between the fundamental mode C stars and the extreme (redder) fundamental mode C0x stars, and so they are treated separately in Section 5.1 and Appendix A. However, in Section 5.2 it is clear that the physical properties— L , M , P and R —do not separate these stars from the others, and so they are more appropriately binned together and understood to be two parts of the same population.

3.1. Dust-to-Gas Ratio and Mass-Loss Rates

Dust mass-loss rates are provided in the Riebel et al. (2012) database, based on fitting to models in the GRAMS grid. For ease of comparison to other works, we want the total mass-loss rate of the stars. However, the exact relation between the dust mass-loss rate, \dot{M}_{dust} , and the gas mass-loss rate, \dot{M}_{gas} , (and combined, the total mass-loss rate \dot{M}) depend on factors that are not well known (van Loon 2000). Therefore, we will select values based on the final equations in van Loon (2000), but will also examine the consequences if the actual ratio differs from these values in Section 7

$$\log \psi_M = 0.7^{+0.6}_{-0.3} \log Z/Z_\odot + \text{constant}_M \quad (8)$$

$$\log \psi_C = 1.0^{+0.3}_{-0.3} \log Z/Z_\odot + \text{constant}_C. \quad (9)$$

Here, ψ is the dust-to-gas ratio and Z is the metallicity of the star. The constants in these equations are unknown, but we know approximately the value for stars of solar metallicity: 500 and 200, respectively (Spitzer 1978; Gullieuszik et al. 2012; Riebel et al. 2012), which are noted here as well as in van Loon et al. (2008) as being a poor fit for the low metallicity stars in the LMC. Using these values to calibrate, we found $1/\psi_M \approx 2913$ ($\text{constant}_M = -\log 500$) and $1/\psi_C \approx 2480$ ($\text{constant}_C = -\log 200$) while using $Z = 0.001$, consistent with the star formation history found by Harris & Zaritsky (2009) and what seems to be necessary to replicate the total mass-loss rates derived by Pastorelli et al. (2020) using these dust-to-gas ratios. These larger ratios also bring the mass-loss rates into the same range as seen in solar metallicity stars, consistent with the results of McDonald et al. (2018) which see mass-loss as being essentially independent of metallicity. This scaling can easily be undone or adjusted when this relationship is better understood.

Figure 3 displays histograms of \dot{M}/M , chosen because $\dot{M}_{\text{crit.}} = M/t_{\text{ev}}$. This lets us indicate the location of the death line in the samples. As explained in Section 1, we will be using an evolution time of 3.2 Myr; thus, at the death line, $\log(\dot{M}/M) = -6.5$. In all four cases, with this t_{ev} value, the stars are clustered close to the death line and a majority are found in the death zone (defined as ± 1 dex in $\log \dot{M}/M$ from the death line). The decrease in the histogram for mass-loss rates above the critical mass-loss rate is expected from the more rapid evolution once M is decreasing quickly. The decline on the low mass loss side is presumed to be the result of a combination of lower mass-loss rates producing less dust, lower mass-loss rates being harder to detect, and (given the intrinsic scatter in the mass-loss rates) our exclusion of stars with derived mass-loss rates below $10^{-8} M_\odot/\text{yr}$. The lower mass-loss rate stars may also show lower amplitude light curves and miss being included because we only included stars with a measured period.

The strong conclusion from these histograms is that in all four categories, the stars populate the death zone, and thus, a star does not need to be in a particular mode of pulsation to lose its envelope as an AGB star, though an overtone pulsator will do so at a slightly higher L . In fact, to reach and populate the overtone strip, a star must avoid being in the fundamental mode when it passes through the fundamental mode death zone, or it must avoid passing through the fundamental mode death zone, for example through an episode of rapid mass loss.

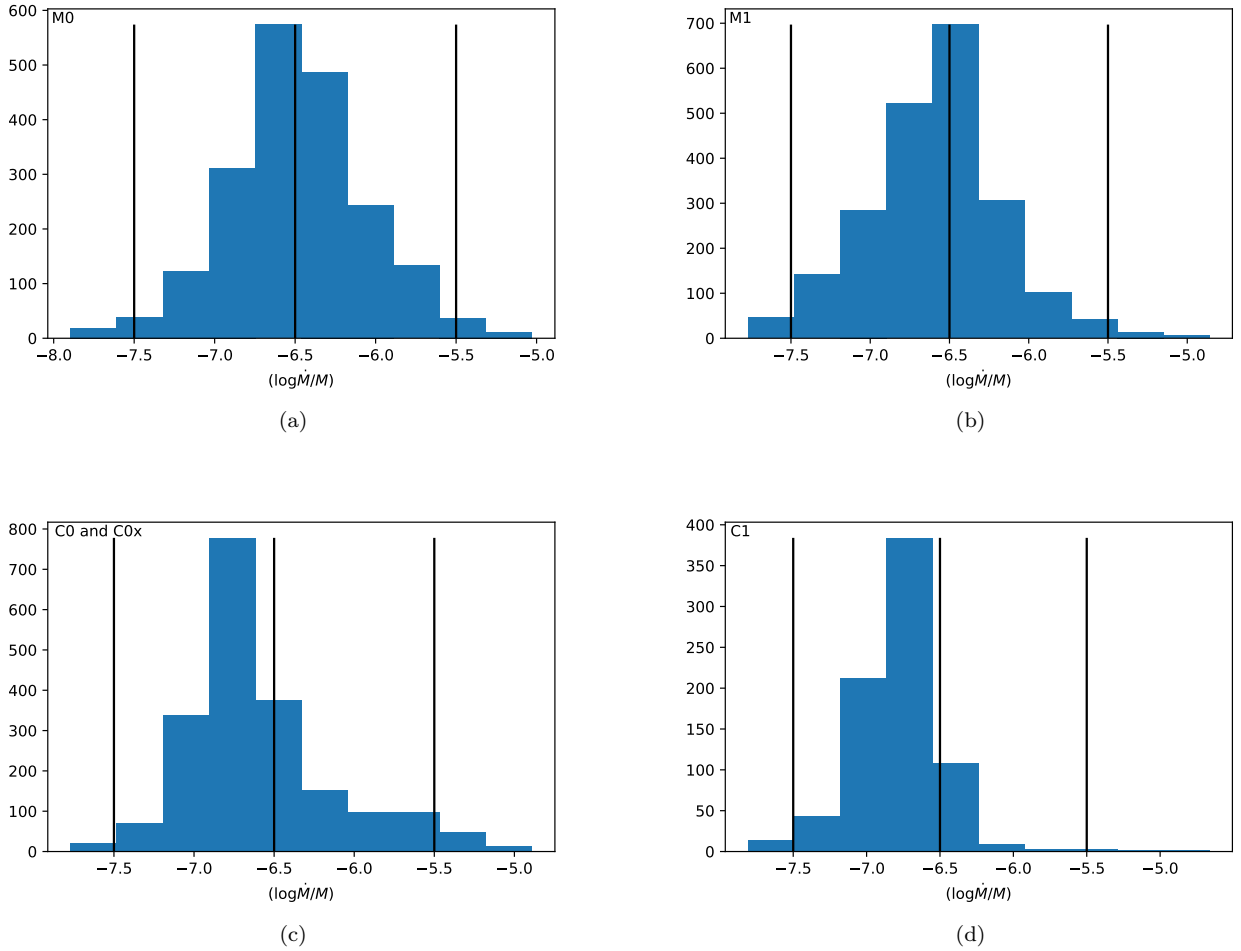


Figure 3. The distribution of $\log(\dot{M}/M)$ showing the death line ($\dot{M}/M = 1/t_{ev}$) and the death zone ($\dot{M}/M = 1/t_{ev} \pm 1$). The drop off above the death line results from rapid evolution at high mass-loss rates. The drop off below the death line is presumed to be due to the difficulty of measuring lower dust mass-loss rates and/or a lower dust-to-gas ratio at low mass-loss rates.

4. OBTAINING R AND M THROUGH MODEL GRIDS

For our bilinear fits, we will be using the observed quantities \dot{M} , L , and P . To put these results into the context of stellar evolution, we will need to derive the mass M and radius R for each star as well. Here, we find evolutionary tracks $R(L, M)$ and period-mass-radius relations $P(M, R)$. We have $P(M, R)$ and $R(L, M)$ relations (*cf.* Iben (1984); Trabucchi et al. (2019); Fox & Wood (1982); Ostlie & Cox (1986)), but they either need to be re-assessed using modern results or utilize parameters that are simply not found in the (Riebel et al. 2012) data set. We will need these variables and relations to analyze the distribution in L and M and for comparison to other formulae. Going forward, we will be assuming that the photospheric radius (found from evolutionary models) and the pulsation radius (used in the period-mass-radius relation) coincide.

4.1. Radius-Mass-Luminosity Relations

Evolutionary models tell us what radius and luminosity to expect for a star of mass M and the fractional metallicity Z at a given evolutionary stage. For AGB stars, the radius depends on the choice of mixing length parameter; for a grid of models this is usually tuned by forcing the models to fit the present day Sun and/or to produce isochrones that fit observations of clusters. Earlier work (e.g. Bowen & Willson (1991)) used relationships from Iben (1984). For this work, we will use the PARSEC-COLIBRI isochrones (Bressan et al. 2012; Marigo et al. 2013; Tang et al. 2014; Pastorelli et al. 2020) to find a set of evolutionary tracks $R(L, M)$ for a composition appropriate for AGB stars in

the LMC, while also separating M-type and C-type stars. We used isochrones in intervals of $\Delta \log t = 0.05$ between $\log t = 8.0$ and $\log t = 10.1$ years. AGB stars were then selected by choosing isochrone stars with $\log(L/L_\odot)$ between 2.9 and 4.2 that have a listed pulsation period or periods.

For our analysis, we chose isochrones for stars with metallicity $Z = 0.003$, similar to the metallicity found in the LMC 10 Gyr before present (see [Harris & Zaritsky 2009](#), Figure 11), representing a typical age for the stars in our sample. We have not determined if there is a metallicity dependence in the radius-luminosity-mass relations, and leave that for a more dedicated analysis than what is here. Using these isochrones, we found a power law fit to the equation:

$$\log R = \log A_{RLM} + B_{RLM} \log L + C_{RLM} \log M. \quad (10)$$

The results of these fits can be found in Table 2. Prior work (e.g. [Bowen & Willson \(1991\)](#)) used a formula from [Iben \(1984\)](#) that had mixing length as a free parameter and a change of slope $d \log R / d \log M$ at $M = 1.175$. Our new fits to the isochrone data are based on models with calibrated mixing length and the above metallicity, and show no discontinuity in the slope. Note that this metallicity is slightly different from the value used in Section 3.1 because this was the nearest value available in the TP-AGB isochrone grids when we did this work. Graphical comparisons of our results to [Iben \(1984\)](#) can be found in Figure 4. Our relation for M stars agrees well with the luminosity dependence of the [Iben \(1984\)](#) relation when the mixing length is 1.1; the same is true for the C stars when mixing length is 0.7 or 0.9, depending on the luminosity. The mass dependence is significantly different between C/O compositions.

Table 2. Fit of $\log R = \log A_{RLM} + B_{RLM} \log L + C_{RLM} \log M$

Composition	$\log A_{RLM}$	B_{RLM}	C_{RLM}
M	-0.241(9)	0.690(3)	-0.251(4)
C	-0.323(27)	0.737(7)	-0.371(14)

NOTE— R , L , and M are measured in solar units. Values in parentheses are the uncertainty, using standard error. Z was taken to be 0.003, consistent with AGB stars formed in the LMC 8.5 to 10.5 Gyr before present (see [Harris & Zaritsky 2009](#), Figure 11).

4.2. Pulsation-Mass-Radius Relations

We now need a pulsation-mass-radius relation to determine the mass of these stars (e.g., [Fox & Wood 1982](#); [Ostlie & Cox 1986](#)). [Trabucchi et al. \(2019\)](#) have done an extensive study of pulsation for long period variables, extending over a greater parameter range than our data. Their formula for overtone pulsation is very similar to that found in previous works, and the formulas are reproduced in Table 3.

For the fundamental mode, [Trabucchi et al. \(2019\)](#) give a non-linear multi-parameter fitting formula:

$$\begin{aligned} \log P = & a_0 + a_M \log M + a_R \log R + b_M (\log M)^2 + b_{MR} \log M \log R + b_R (\log R)^2 \\ & + c_M (\log M)^3 + c_{MR} (\log M)^2 \log R + c_{RM} \log M (\log R)^2 + c_R (\log R)^3 \\ & + a_Z \log Z + a_Y Y + a_{C/O} \log \left[\frac{C/O}{(C/O)_{\text{ref}}} \right]. \end{aligned} \quad (11)$$

The [Riebel et al. \(2012\)](#) data set lacks information on helium content Y and metallicity Z , so we must assume a reasonable value for the entire data set; as before we took isochrones of $Z = 0.003$ which we then algebraically adjusted to $Z = 0.001$ and now $Y = 0.28 - Z$. As explained in [Trabucchi et al. \(2019\)](#) and [Trabucchi et al. \(2021\)](#), fitting a fundamental-mode pulsation formula over a wide range of parameters is very difficult due to complex dependence on M and R and the relationship is non-linear over the full parameter range ($0.6 < \log P < 3.8$). However, as noted in

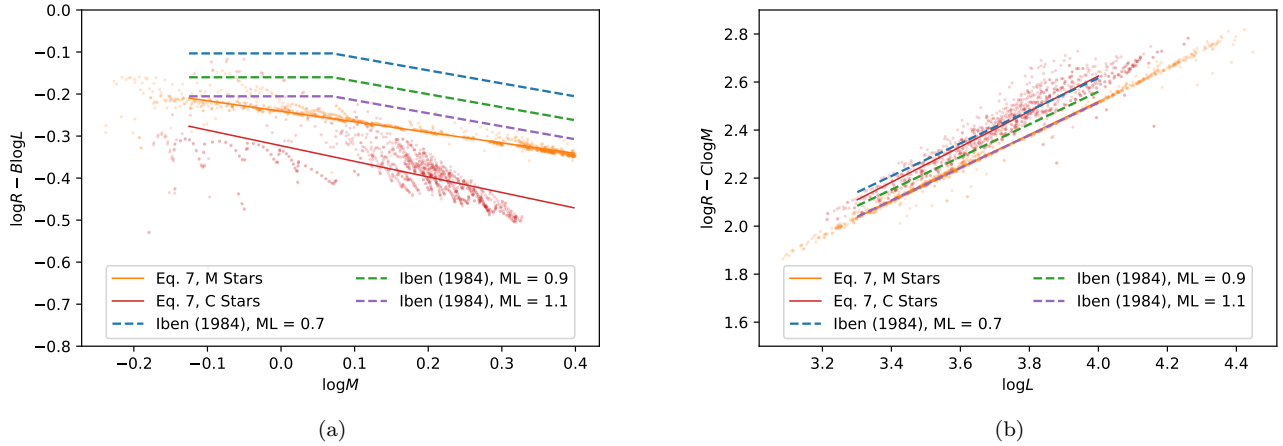


Figure 4. To project this three-dimensional fit into two dimensions, (a) has had the luminosity dependence of the relations removed and (b) has had the mass dependence removed. Same color dots show the models that were used to determine the relations, color matched to the fits.

Trabucchi et al. (2021) and as we can see in Figure 5, a linear relationship is sufficient when $\log R < 2.4$ for the M0 stars (only one M0 star in our data set is larger), and as noted in Trabucchi et al. (2019) a linear relationship has errors of up to 20% for the C0 stars. Thus, we have both the fundamental and overtone mode relations in the form:

$$\log P = \log A_{PMR} + B_{PMR} \log M + C_{PMR} \log R + D_{PMR} \log \frac{Z}{0.003} + E_{PMR}(0.003 - Z), \quad (12)$$

noting that this relation is calibrated with the chosen isochrone metallicity $Z = 0.003$ and the helium content being $Y = 0.28 - 0.003 = 0.277$. This relation for first-overtone stars is valid up to 250 days, after which it becomes less precise (Trabucchi et al. 2019). We have applied this relation to 26 of our C1 stars that have periods longer than 250 days, however they make up a small part of the sample. The results for the fundamental modes can be found in Table 3, with the fundamental mode results being in slightly better agreement with the results of Fox & Wood (1982) and the overtone mode results being in agreement with Ostlie & Cox (1986). These are good fits to the periods derived from the Trabucchi et al. (2019) formula (eq. 12). Ideally, this fit would be done with the original models that fell within our range of parameters, because their formula may not be an ideal fit in that subset of parameter space. A graphical comparison of the PMR relations described here and those found in Fox & Wood (1982) and Ostlie & Cox (1986) can be seen in Figure 5.

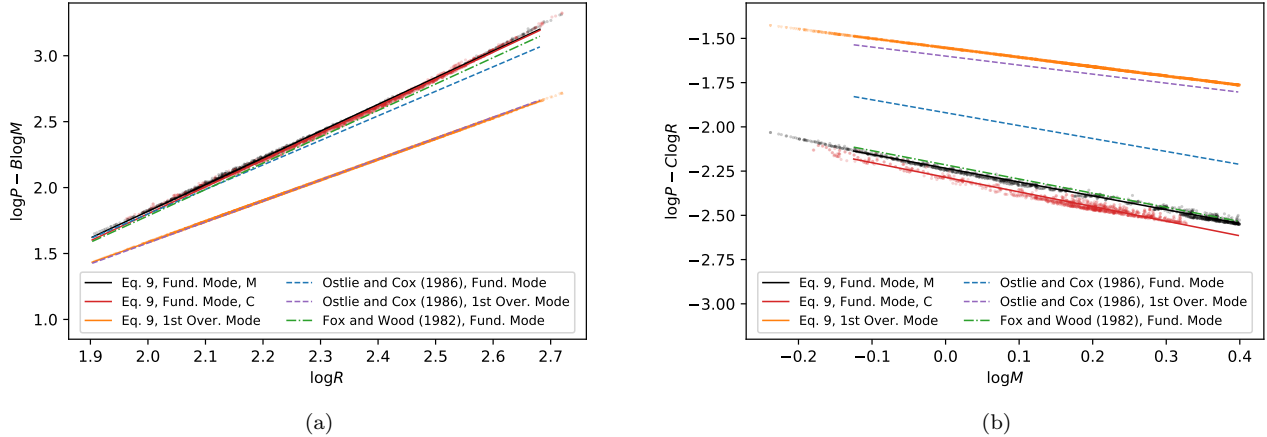


Figure 5. Comparison of the Pulsation-Mass-Radius (PMR) relations found in this work and [Trabucchi et al. \(2019\)](#) (solid lines, black for M0, red for C0, and orange for first-overtone) compared to the frequently used relations from [Fox & Wood \(1982\)](#) (dotted-dashed) and [Ostlie & Cox \(1986\)](#) (dashed; blue for fundamental mode, purple for first-overtone mode). (a) has had the mass dependence of the relations removed and (b) has had the radius dependence removed, to project a three-dimensional fit into two dimensions. The models used to determine the relations are marked as same color dots on each plot. Note that neither the Fox and Wood formula nor the two Ostlie and Cox formulae distinguish M- and C-stars. While this does not seem to have a significant impact on the relation between pulsation period and radius, we can see a distinct offset when comparing pulsation period and mass. The radius dependence of all formulae are in general agreement with each other. The mass dependence of the formulae are generally in agreement, but with different scaling coefficients; the first-overtone formulae have a small difference while our fundamental mode formulae agree much better with the Fox and Wood formula than the Ostlie and Cox formula.

5. MASS-LOSS RATES FROM STELLAR PARAMETERS

The ultimate goal of this work is to find reliable formulae for mass-loss rates for AGB stars in terms of stellar parameters (L, P) or (L, M) , making use of the extensive data on AGB stars in the LMC. The first widely used formula, from [Reimers \(1975\)](#), expressed mass-loss rate as a power law of luminosity, mass, and radius: $\dot{M} \sim LR/M$. Other power law formulations followed: [Goldberg \(1979\)](#); [Blöcker \(1995\)](#); [Wachter et al. \(2002\)](#). [Vassiliadis & Wood \(1993\)](#) fitted an exponential dependence on period P . The formulae based on observations tend to be less steep — that is, to have smaller exponents — than those found from mass-loss modeling (e.g. [Bowen \(1988\)](#); [Bowen & Willson](#)

Table 3. Fit of $\log P = \log A_{PMR} + B_{PMR} \log M + C_{PMR} \log R + D_{PMR} \log Z / 0.003 + E_{PMR} (0.003 - Z)$

Subset	$\log A_{PMR}$	B_{PMR}	C_{PMR}	D_{PMR}	E_{PMR}
M0	-2.234(5)	-0.7802(2)	2.027(2)	-0.02713	0.14872
M1	-1.554(4)	-0.529(1)	1.570(1)		
C0	-2.285(7)	-0.826(4)	2.043(3)	-0.02713	0.14872
C1	-1.554(4)	-0.529(1)	1.570(1)		

NOTE— R and M are measured in solar units, P is measured in days. Isochrones with metallicity Z were $Z = 0.003$, used to find these relations. The metallicity adjustments are assumed to be the same as in [Trabucchi et al. \(2019\)](#), and are calibrated here for the chosen isochrone metallicity and a helium content $Y = 0.28 - 0.003 = 0.277$. Values in parentheses are the uncertainty, using standard error.

(1991); Winters et al. (2000); Willson et al. (2008); Wang et al. (2009); Bladh et al. (2019a,b)). We will compare our results with these earlier formulae in Section 6.

Our standard bilinear fits, described in Section 5.1, overestimate low mass-loss rates and underestimate high-mass-loss rates. This is characteristic of most of the other published formulae, as we will see in Section 6. By fitting with $\log L$ as the dependent variable, we show that this is consistent with regression dilution (Spearman 1904; Frost & Thompson 2000; Carroll et al. 2006), a phenomenon that occurs when the scatter in one or more of the independent variables (in this case, L) are too large.

In section 5.2, we have developed an independent method for deriving the exponents from the distribution of the stars in the $\log L$, $\log P$ -plane. This method directly relates the distribution of stars in this plane to the exponents of a power law mass-loss formula, and by construction maintains a constant quality-of-fit. This method yields significantly larger exponents than a simple linear fit to $\log \dot{M}(\log L, \log P)$ while providing a relation with far less spread than a fit to $\log L(\log \dot{M}, \log P)$. In all cases, the data set has been separated into the five mode and spectral-class based categories established in Section 3.

5.1. Mass-loss rate found via multi-linear regression

First, we used a multi-linear least-squares regression to obtain mass-loss rate formulae for AGB stars, using the method built into the Python “statsmodels” package (Seabold & Perktold 2010) and fitting to the equation:

$$\log \dot{M} = \log A_{\dot{M}LP} + B_{\dot{M}LP} \log L + C_{\dot{M}LP} \log P. \quad (13)$$

In this fit and continuing forward, \dot{M} is the total mass-loss rate. It was calculated using the dust-to-gas ratio determined using equations 8 and 9, with the dust mass-loss rate being that found by fitting GRAMS models to the AGB stars in the LMC by Riebel et al. (2012). We discuss in more detail why these values were chosen in Section 3. Graphical depictions of these fits can be found in Figure 6.

A reliable fit should be reproducible when we switch our dependent and independent variables; otherwise, we will need to look to other methods for verification. The refined MACHO measurements have a frequency-space error of 0.00003 day^{-1} (Fraser et al. 2008). This corresponds to pulsation period errors of between 0.09% and 2.5% for the stars in our selection, with a median error of 0.49%, *i.e.* are relatively small. We note that individual period errors may be significantly larger, especially in the case of sparse data; verifying these periods is beyond the scope of this paper. However, this is not the case for luminosity or mass-loss rate. We first use luminosity as our dependent variable, and fit the equation:

$$\log L = \log \alpha_{L\dot{M}P} + \beta_{L\dot{M}P} \log \dot{M} + \gamma_{L\dot{M}P} \log P. \quad (14)$$

We then algebraically solve for \dot{M} to have the same form as equation 13, a function of the best fit coefficients:

$$\log \dot{M} = \log A_{L\dot{M}P} + B_{L\dot{M}P} \log L + C_{L\dot{M}P} \log P, \quad (15)$$

where $\log A_{L\dot{M}P} \equiv -\log \alpha_{L\dot{M}P} / \beta_{L\dot{M}P}$, $B_{L\dot{M}P} \equiv 1 / \beta_{L\dot{M}P}$, and $C_{L\dot{M}P} \equiv -\gamma_{L\dot{M}P} / \beta_{L\dot{M}P}$. This procedure results in drastically different values for our exponents. This suggests there is a significant amount of regression dilution occurring. Regression dilution occurs due to the large uncertainties in the independent variable, here the luminosity as reported by Riebel et al. (2012). The results of these fits for our five populations of stars—M0, M1, C0, C0x, and C1—can be found in Table 4. A graphical comparison of the quality of these two linear fits and the method discussed in Section 5.2 can be found in Figure 9.

The natural next step would be to attempt to correct for the regression dilution in some standard way. However, there are several reasons why that approach does not work in this case. Overall, correction is complicated by the data having differential error. The first method attempted was an orthogonal regression, but this method is only valid in cases of multiple independent variables. This problem has multiple interdependent variables (L , P , M , and R) all of which are connected by the relations found in Section 4. The angular bisector of the two linear fits also fails as a solution because it forces exponents to be between those found in the fits—as we will see in Sections 5.2 and 6, better solutions are outside this range. Finally, data correction methods for the set fail due to the current state of the problem—we are attempting to determine the known relation here and we lack covariances for the errors (Carroll et al. 2006).

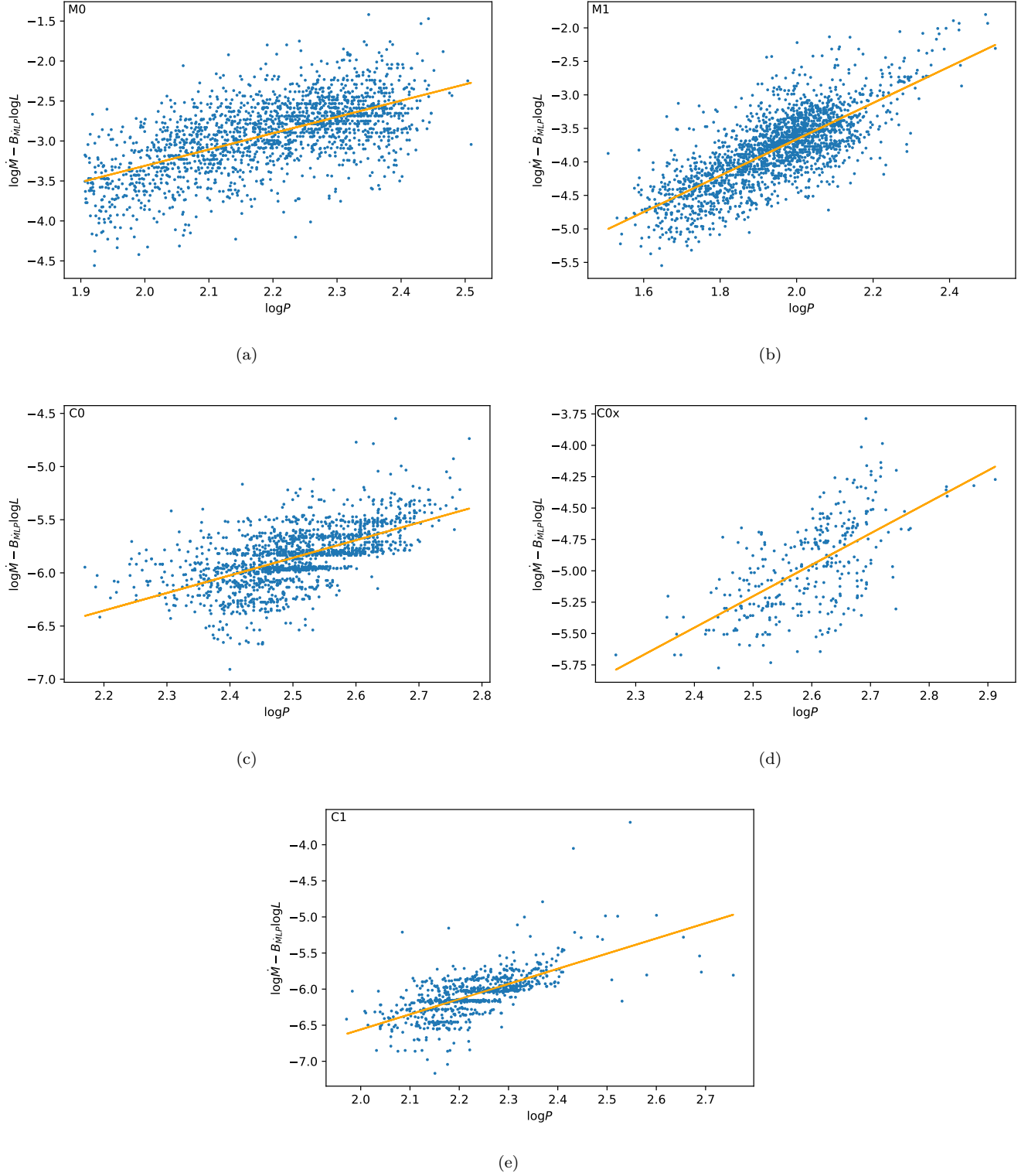


Figure 6. The quality of the fit of our mass-loss rate formula $\log \dot{M} = \log A_{MLP} + B_{MLP} \log L + C_{MLP} \log P$ from equation 13 for our five combinations of spectral class and pulsation mode. On the x -axis is $\log P$ and on the y -axis is $\log \dot{M} - B_{MLP} \log L$. The full details of each fit can be found in Table 4. Despite the least-squares fit working as intended, we will see in Section 6 that these fits are experiencing regression dilution.

Table 4. Fit of $\log \dot{M} = \log A + B \log L + C \log P$

Subset	$\log A_{MLP}$	B_{MLP}	C_{MLP}	$\log A_{LMP}$	B_{LMP}	C_{LMP}
M0	-7.4(2)	-1.01(7)	2.04(9)	8(1)	-12.3(9)	12(1)
M1	-9.1(1)	-0.77(9)	2.7(1)	12(2)	-24(3)	35(4)
C0	-10.0(1)	-0.28(5)	1.66(8)	4(2)	-15(3)	18(3)
C0x	-1.0(3)	-0.04(2)	1.75(8)	-25(14)	-24(12)	42(21)
C0, C0x	-11.4(2)	-1.16(6)	3.6(1)	-4.1(8)	-7.3(4)	10.0(6)
C1	-10.8(2)	-0.22(8)	2.1(1)	24(10)	-22(8)	25(9)

NOTE—Comparison of results of fitting $\dot{M}(L, P)$ and translating a fit of $L(\dot{M}, P)$. \dot{M} is measured in solar masses per year, L is measured in solar units, and P is measured in days. \dot{M} is taken to be the dust mass-loss rate multiplied by the inverse of the dust-to-gas ratio ψ (see Section 3). Values in parentheses are the uncertainty, using standard error. As C0x appear to be the C0 stars undergoing the highest mass-loss rates, they are also analyzed together.

5.2. Mass-loss Rate found from the PL strip

We can use the distribution of AGB stars in the $\log P$, $\log L$ plane as an alternative way to estimate the exponents of a mass-loss formula in those two variables. The general behavior of AGB stars in this plane is described in Figure 2 of Bowen & Willson (1991), and Figure 7 of Willson (2000). At the beginning of the AGB these stars present low mass-loss rates barely affecting their total mass, while their core grows due to shell burning, causing their luminosity to increase. In this phase, the stars move horizontally in the diagram (roughly constant M with increasing L). This initial trend eventually comes to an end, as finally the mass-loss rate increases to a point that the total mass of the star is significantly affected on timescales shorter than the luminosity increase driven by the slower nuclear timescales. In this phase, the stars move roughly vertically in the $\log L$, $\log M$ plane (roughly constant L with rapidly decreasing M). The occurrence of thermal pulses during the TP-AGB phase, as well as the dynamical processes of dust formation in the circumstellar envelope, introduce scatter to these idealized trajectories, as luminosity and mass-loss rate can change significantly over the short timescales of the He-shell burning. The longer and more stable inter-pulse quiescent phases are however well characterized by this general behavior.

A sample of AGB stars selected on the basis of having a reliable determination of their mass-loss rate (such as our LMC samples) will spread on the L , M plane along the trajectories described above. Their distribution, however, will be limited to a relatively narrow strip (LM strip hereafter) at the interface between the low and high mass loss phases in their AGB evolution. The region above the strip will be sparsely populated because their lower mass-loss rate will be below the minimum threshold set for a reliable determination of this parameter. The region below the strip will also be depleted because stars in this area evolve too quickly out of the AGB to be detected in any significant number. When we plot P vs. L the stars form a similar strip (PL strip hereafter) where stars progress upwards and to the right as luminosity and pulsation period increase over time. In this arrangement, stars below the strip have mass-loss rates that are hard to measure while stars above are evolving off the AGB quickly.

With the relations described in Section 4, we have a pair of linear transformations, which means we will obtain the same result whether we perform the analysis in $\log L$, $\log M$ or $\log L$, $\log P$. We are choosing to perform this analysis in $\log L$, $\log P$ because this method uses the untransformed observational data, and so the resulting $\log L$, $\log M$ formulae can be updated as our understanding of the RML and PMR relations improves. This is shown in Figure 7 and 8 for our samples of LMC AGB stars with different envelope chemistry and pulsation modes.

The black solid line shown in Figure 7, which we derived by fitting the $\log L$ and $\log P$ data in each strip, traces the location where the star’s behavior changes from the low to high mass loss phases described above. This fit line is a good approximation of the “the cliff” described in Bowen & Willson (1991), as can be seen in Figure 8.

The conclusion that a majority of the stars are in the death zone only depends on the distribution of the observed mass-loss rates in $\log \dot{M}/M$ and the chosen evolution time or critical mass-loss rate. As argued in Section 1, t_{ev} should range between 1.2 and 1.7 Myr, which does not push a majority of stars out of the death zone at either extreme. The extremes of the dust-to-gas ratio (see equations 8 and 9) also allow bulk shifts of $\log(\dot{M}/M)$ by -0.65 to 0.33 , which is

also insufficient move them outside the death zone. It does not depend on the derived mass-loss formulae, the derived stellar masses and radii, or even the observed periods.

Mass-loss rates increase with increasing L or decreasing M , leading to a narrow strip in LM space. The transformation to PL is linear, thus we also have a narrow strip in PL space. If the mass-loss rate increases monotonically as L increases or as M decreases (as implied by one- or two-parameter mass-loss rate formulae), then the width of the LM strip depends on how steeply the mass-loss rate increases as a star evolves along the AGB. Therefore, for a power law mass-loss formula, larger exponents imply narrower distributions. It follows then that by measuring the width and height of the band the stars occupy in $\log M$ versus $\log L$ space we can derive a lower limit on the size of the exponents. Absent an overly-restrictive definition of the band, this is a lower limit because any random errors in the measurements will tend to broaden the distribution, so the error-free distribution is as narrow as or narrower than what we find from the observational data. This behavior also means that only stars in this region have a well-defined mass-loss law. Outside the strip, mass-loss is either too low to effectively be tied with certainty to any of our variables or is in the end phase of AGB evolution where behavior is much more dependent on unobserved variables. As long as we have a unique relation between L , M and L , P we can perform the same analysis in P vs. L .

Our general power law formula has the form:

$$\log \dot{M} = \log A_{MLP} + B_{MLP} \log L + C_{MLP} \log P. \quad (16)$$

By taking the partial derivatives with respect to $\log \dot{M}$, we can show:

$$B_{MLP} = \frac{\partial \log \dot{M}}{\partial \log L} \approx \frac{\Delta \log \dot{M}}{\Delta \log L} \quad (17)$$

$$C_{MLP} = \frac{\partial \log \dot{M}}{\partial \log P} \approx \frac{\Delta \log \dot{M}}{\Delta \log P} \quad (18)$$

where $\Delta \log L$ and $\Delta \log P$ are the ranges of luminosity and mass when keeping the other fixed — thus, the width and height of PL strip, respectively. For each class of stars, the observations yield a range of mass-loss rates: $\Delta \log \dot{M}$.

To apply this, we need to precisely define the strip as well as measure the range of mass-loss rates of stars in the strip, excluding any major outliers. We will first find the line that best fits the $\log P$ and $\log L$ data.

$$\log P = \alpha \log L + \beta \quad (19)$$

The PL strip is defined to be bound in $\log L$ - $\log P$ space by lines $\pm n$ times the standard deviation σ_{FL} of the points around the best fit line. This makes n our fitting variable. The width $\Delta \log L$ and height $\Delta \log P$ can then be calculated algebraically using the lines bounding the strip.

$$\Delta \log P \equiv 2n\sigma_{FL} \cos(\tan^{-1} \alpha) \quad (20)$$

$$\Delta \log L \equiv \frac{\Delta \log P}{\alpha} \quad (21)$$

This fixes the ratio of B and C to α , the slope of the strip's best-fit line. We estimate the range of \dot{M} as the 95% of stars closest to the mean mass-loss rate; this accounts for a majority of the range while cutting the most extreme outliers. This gives $\Delta \log \dot{M} \approx 1.7$ for each set except for C1, where it is about 1.3; exact values can be found in Table 5. $\Delta \log \dot{M}$ does not change predictably with n , so we must determine n by testing different values; for each subset, we checked $0.5 \leq n \leq 3.0$, in steps of 0.0001. The final value of n for each subset stars is whichever value brings the linear fit of $\log \dot{M}_{\text{calc.}}$ vs $\log \dot{M}_{\text{obsv.}}$ closest to a slope of 1. The scaling coefficient A can be determined by forcing the mean residual of $\log \dot{M}$ to be zero.

The results of this method can be found in Table 5. Comparing these results to those we found in Section 5.1, we can see that the PL Strip method produces large exponents like the indirect linear fit of $\log L(\log \dot{M}, \log P)$, in contrast to the smaller exponents of the direct fit of $\log \dot{M}(\log L, \log P)$. This is further discussed in Section 6 and in Table 7 within.

Table 5. PL Strip Analysis of [Riebel et al. \(2012\)](#) Data Set

Sample	α	β	n_{fit}	Stars in Strip	$\Delta \log P$	$\Delta \log L$	$\Delta \log \dot{M}$	$\log A_{MLP}$	$\log B_{MLP}$	$\log C_{MLP}$
M0	0.63	-0.01	1.06	1,237	0.15	0.24	1.62	-6.63	-6.67	10.7
M1	0.63	-0.30	0.89	1,207	0.09	0.14	1.92	-0.26	-13.9	22.2
C0 & C0x	0.41	0.96	1.51	1,668	0.21	0.52	1.88	-14.7	-3.59	8.77
C1	0.46	0.44	1.16	619	0.15	0.31	1.24	-10.1	-3.94	8.49

NOTE— L and M are measured in solar units. Exponents B and C are associated with Equation 16. As C0x appear to be the C0 stars undergoing the highest mass-loss, they are analyzed together. For further detail, see Section 5.2.

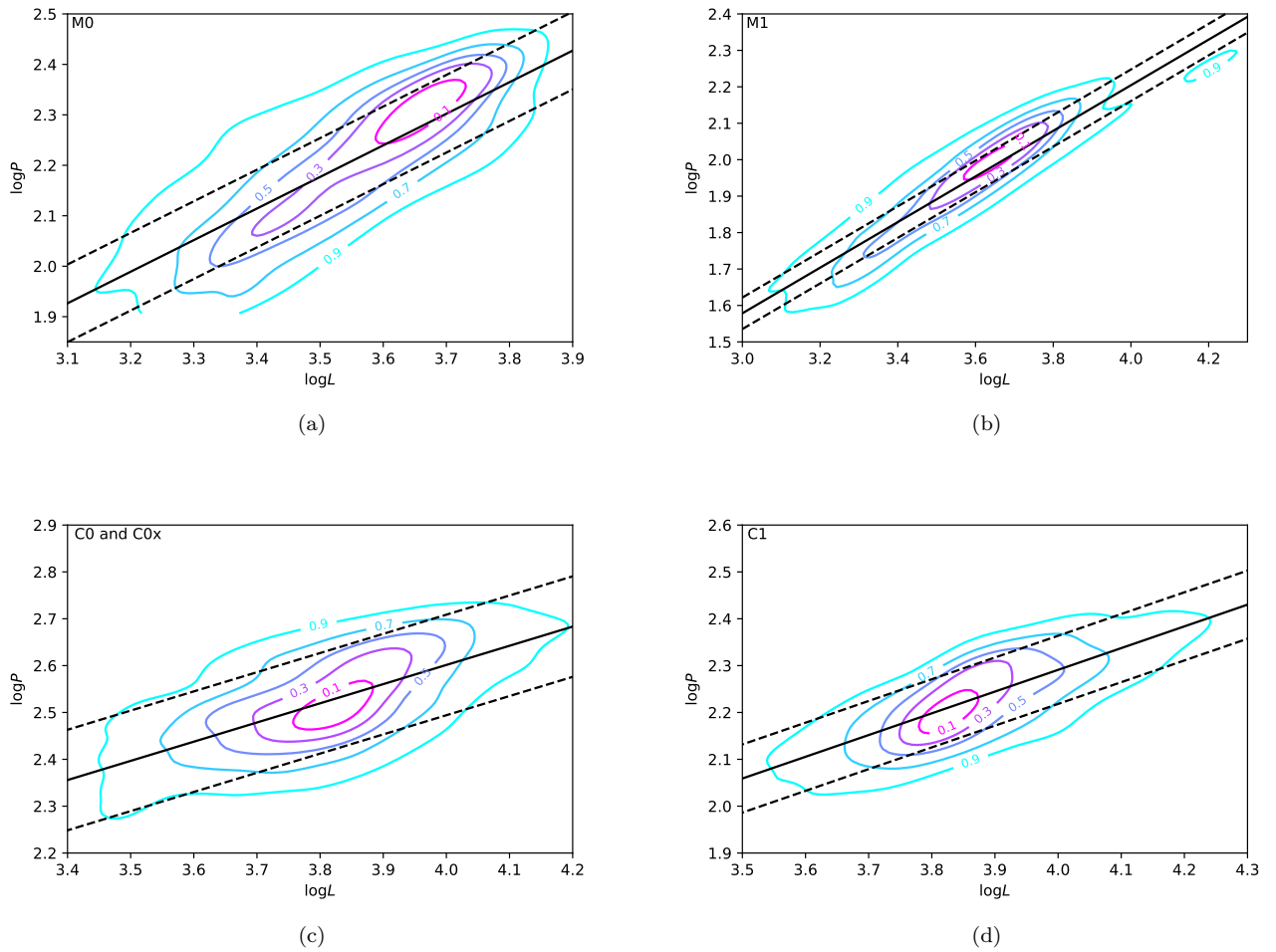


Figure 7. Stars in the PL strip in the [Riebel et al. \(2012\)](#) data set, split into five spectral type and pulsation mode categories as indicated on the figures and as detailed in Section 5.2. The black solid line is the best-fit line of each data set, and the black dashed lines bound the stars in the best-fitting strip, with their width and height given in Table 5. Contours depict the fraction of stars relative to the peak density.

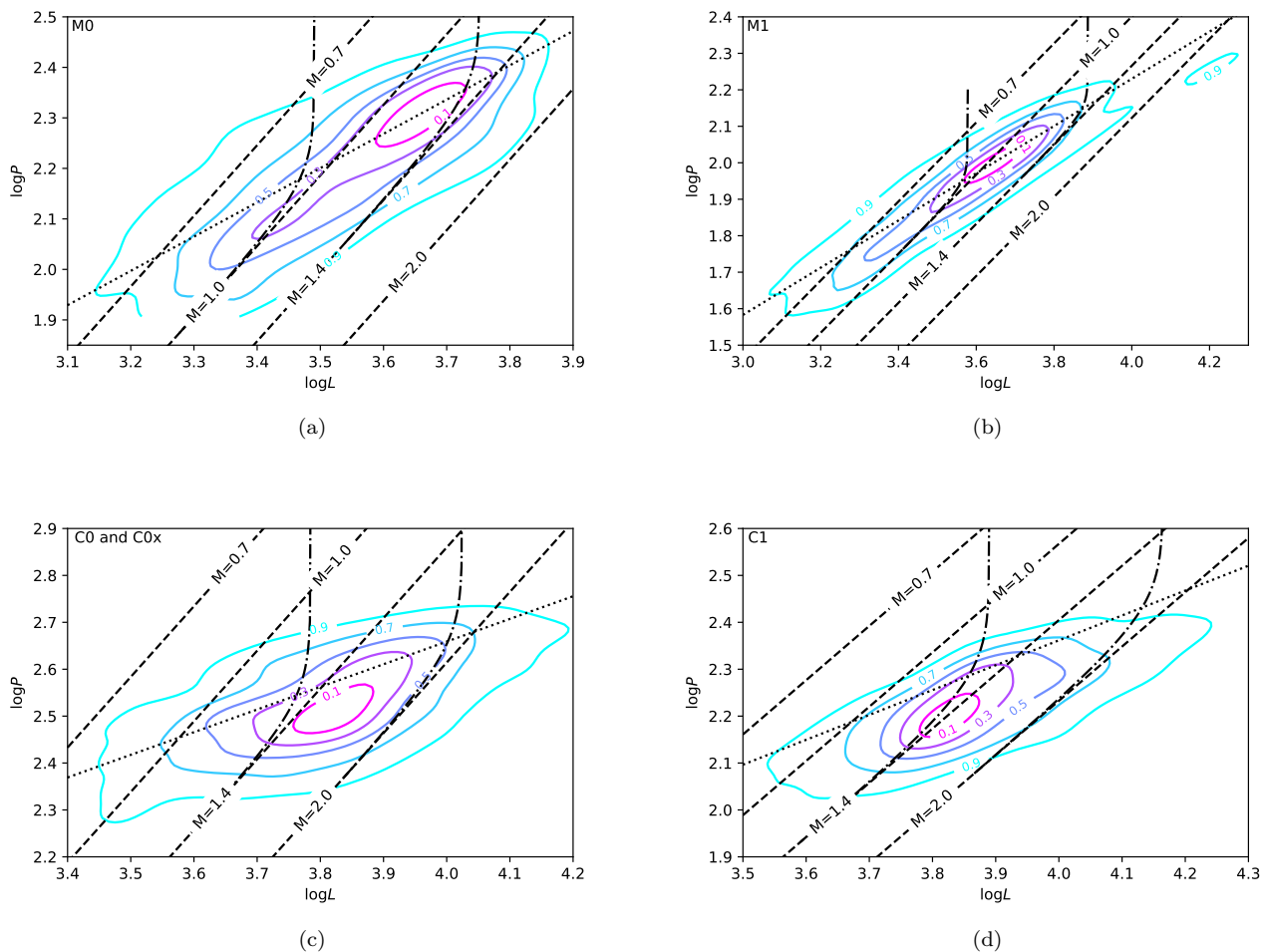


Figure 8. The evolution of the stars using the derived mass loss formulae (Eq. 16, Table 5) is superimposed on the distribution (contours) with the death line indicated (dotted line). Lines of constant mass (dashed lines) and evolutionary tracks (dot-dashed lines) are also included. The pattern is clear: Before the death line, the mass changes relatively little; after, it is seen to be decreasing. The horizontal axis is also a time axis; $\Delta t = (\Delta \log L / 2.3) * t_{ev}$, so with $t_{ev} = 3.2$ Myr, $\Delta \log L = 0.1$ corresponds to 0.14 Myr.

6. COMPARISON WITH OTHER FORMULAE

In this paper, we have approached the problem of finding an expression for the mass-loss rate as a function of stellar parameters in several different ways, each one applied to five sets of stars. We have found rough agreement between two methods, fitting $L(\dot{M}, L)$ (Section 5.1), and the L, M distribution method (Section 5.2), and an explanation for why direct fitting of \dot{M} as a function of stellar parameters produces a discordant result: regression dilution when one independent parameter has too much scatter. In this section, we look at a variety of published formulae, and show that they also show the signature of regression dilution, confirming our conclusion that errors in L have systematically led to underestimates for the exponents in power law fits for the mass-loss rate.

These formulae do not exist in isolation, so we should examine them in the context of other formulae and other known results. Below, you can find a non-exhaustive list of other observation-based formulae from over the last 45 years.

$$\text{Reimers (1975): } \dot{M} = (4 \times 10^{-13}) \eta \frac{LR}{M} \quad (22)$$

$$\text{Reimers (1977): } \dot{M} = (4 \times 10^{-13}) (0.35) \frac{LR}{M} \quad (23)$$

$$\text{Vassiliadis \& Wood (1993): } \log \dot{M} = \begin{cases} -11.4 + 0.0123P & \text{if } M < 2.5 M_{\odot} \\ -11.4 + 0.0125(P - 100(M - 2.5)) & \text{if } M > 2.5 M_{\odot} \end{cases} \quad (24)$$

$$\text{Blöcker (1995): } \dot{M} = 1.932 \times 10^{-21} \frac{L^{3.7} R}{M^{3.1}} \quad (25)$$

$$\text{van Loon et al. (2005): } \log \dot{M} = -5.65 + 1.05 \log \left(\frac{L}{10^5 L_{\odot}} \right) - 5.3 \log \left(\frac{T}{3500 \text{ K}} \right) \quad (26)$$

$$\text{Schröder \& Cuntz (2005): } \dot{M} = (4 \times 10^{-13}) \eta \frac{LR}{M} \left(\frac{T}{4000 \text{ K}} \right)^{3.5} \left(1 + \frac{g_{\odot}}{g_{\star}} \right) \quad (27)$$

$$\text{De Beck et al. (2010): } \log \dot{M} = \begin{cases} -7.37 + 3.42 \times 10^{-3}(P) & \text{if } P < 850 \text{ d} \\ -4.46 & \text{if } P > 850 \text{ d} \end{cases} \quad (28)$$

In order to compare the various published formulae with each other and with this work, where possible we have used our evolutionary tracks and period-mass-radius relations, together with the definition of effective temperature, to algebraically transform the formulae to a power law in L and M . When this is not possible, we approximated exponents using a bilinear regression in \dot{M} , L , and M , where \dot{M} was calculated with the formula in question for the LMC stars. Our fits also use LMC data, and we do not expect the scaling values ($\log A$) to match across data sets of substantially different metallicity. These comparisons can be found in Table 6.

In Table 7, we can see comparisons of the three formulae we have determined in this paper. The multi-linear fit of $\log \dot{M}(\log L, \log P)$ suffers from a notable issue: underestimating high-mass-loss rates and over-estimating low mass-loss rates with a failure to match the one-to-one line in $\log \dot{M}_{\text{calc.}}$ vs $\log \dot{M}_{\text{obsv.}}$ space. This is the characteristic signature of regression dilution. Except for the Vassiliadis & Wood (1993) formula, which is a fit to the low-noise parameter P , the above listed formula (equations 22–28) all show the same characteristic signature of regression dilution. This issue can be seen clearly if $\log \dot{M}_{\text{calc.}}$ is plotted versus $\log \dot{M}_{\text{obsv.}}$, as we have done in Figure 9 for the formulae in equations 22–28. This issue is circumvented in our PL strip analysis, which finds much better correlation between the calculated and observed values with a similar significance of the fit, as seen by comparing Tables 6 and 7. This result strongly implies that linear fitting methods are suffering from regression dilution, due to both the uncertainty in our measurements of \dot{M} and L and the non-independence of the \dot{M} and L measurements, confirming the suggestions of van Loon et al. (2005); Guandalini et al. (2006); Riebel et al. (2012); and Höfner & Olofsson (2018). Without knowing the reliability of the measurements, we cannot correct for the bias in the linear fits (Spearman 1904; Frost & Thompson 2000; Carroll et al. 2006).

Table 6. Equivalent or Estimated Fit to Function $\log \dot{M} = \log A + B \log L + C \log M$ for Other Formulae

Reference	$\log A$	B	C	Slope of Calc. vs. Obsv. Fit	Std. Dev. of Residual
				M0, M1, C0 and C0x, C1	M0, M1, C0 and C0x, C1
Reimers (1975)	-12.79	1.72	-1.31	0.14, 0.32, 0.13, 0.30	0.38, 0.37, 0.39, 0.24
Vassiliadis & Wood (1993) ^a	-59.0	14.3	-15.1	M0: 1.07, C0: 1.32	M0: 0.34, C0: 0.80
Blöcker (1995)	-21.0	4.39	-3.35	0.35, 0.81, 0.33, 0.77	0.51, 0.54, 0.44, 0.32
van Loon et al. (2005)	5.66	1.73	-0.98	0.12, 0.34, 0.123, 0.31	0.40, 0.38, 0.41, 0.25
Schröder & Cuntz (2005)	-14.7	2.27	-1.81	0.22, 0.46, 0.20, 0.47	0.39, 0.38, 0.31, 0.24
De Beck et al. (2010)	-14.2	2.06	-2.04	0.15, 0.14, 0.37, 0.31	0.37, 0.39, 0.35, 0.24

NOTE— \dot{M} is measured in solar masses per year, L and M are measured in solar units. Exponents are the average of those found using the evolutionary tracks and PMR relations. The second, fifth, and sixth formulae were estimated due to not being power laws.

^a Vassiliadis & Wood (1993) was determined using fundamental-mode stars so is only valid for those subsets of AGBs.

Table 7. Determined Formulae in the form $\log \dot{M} = \log A + B \log L + C \log M$

Subset	Method and Fitting Variables	$\log A_{MLM}$	B_{MLM}	C_{MLM}	$ \frac{B_{MLM}}{C_{MLM}} $	Slope of	σ
						Calc. vs. Obsv.	of Residuals
M0	Linear Fit - $\log \dot{M}(\log L, \log P)$	-12.9	1.85	-2.63	0.70	0.21	0.35
M0	Linear Fit - $\log L(\log \dot{M}, \log P)$	-26.4	5.72	-16.6	0.34	1.00	1.22
M0	PL Strip Method	-35.2	8.24	-13.7	0.59	1.00	0.80
M1	Linear Fit - $\log \dot{M}(\log L, \log P)$	-14.3	2.17	-2.50	0.87	0.34	0.36
M1	Linear Fit - $\log L(\log \dot{M}, \log P)$	-54.8	13.5	-32.1	0.42	1.00	2.00
M1	PL Strip Method	-42.8	10.2	-20.5	0.50	1.00	1.19
C0 and C0x	Linear Fit - $\log \dot{M}(\log L, \log P)$	-21.9	4.23	-5.66	0.75	0.42	0.33
C0 and C0x	Linear Fit - $\log L(\log \dot{M}, \log P)$	-33.6	7.74	-15.8	0.49	1.00	0.82
C0 and C0x	PL Strip Method	-41.0	9.62	-13.9	0.69	1.00	0.52
C1	Linear Fit - $\log \dot{M}(\log L, \log P)$	-15.1	2.21	-2.34	0.94	0.38	0.23
C1	Linear Fit - $\log L(\log \dot{M}, \log P)$	-27.4	6.47	-27.7	0.23	1.00	2.30
C1	PL Strip Method	-27.8	5.89	-9.44	0.62	1.00	0.51

NOTE—For ease of comparison with equations 22–28, all formulae found in this work have been transformed into the form $\dot{M} = AL^B M^C$ using PMR relations and evolutionary tracks of the appropriate kind for spectral class and mode. The PL Strip provides a fit that first works consistently over the entire range of mass-loss rates while also providing a tighter spread than the multi-linear fit to $\log L$. The PL Strip formulae should be taken as the correct formulae.

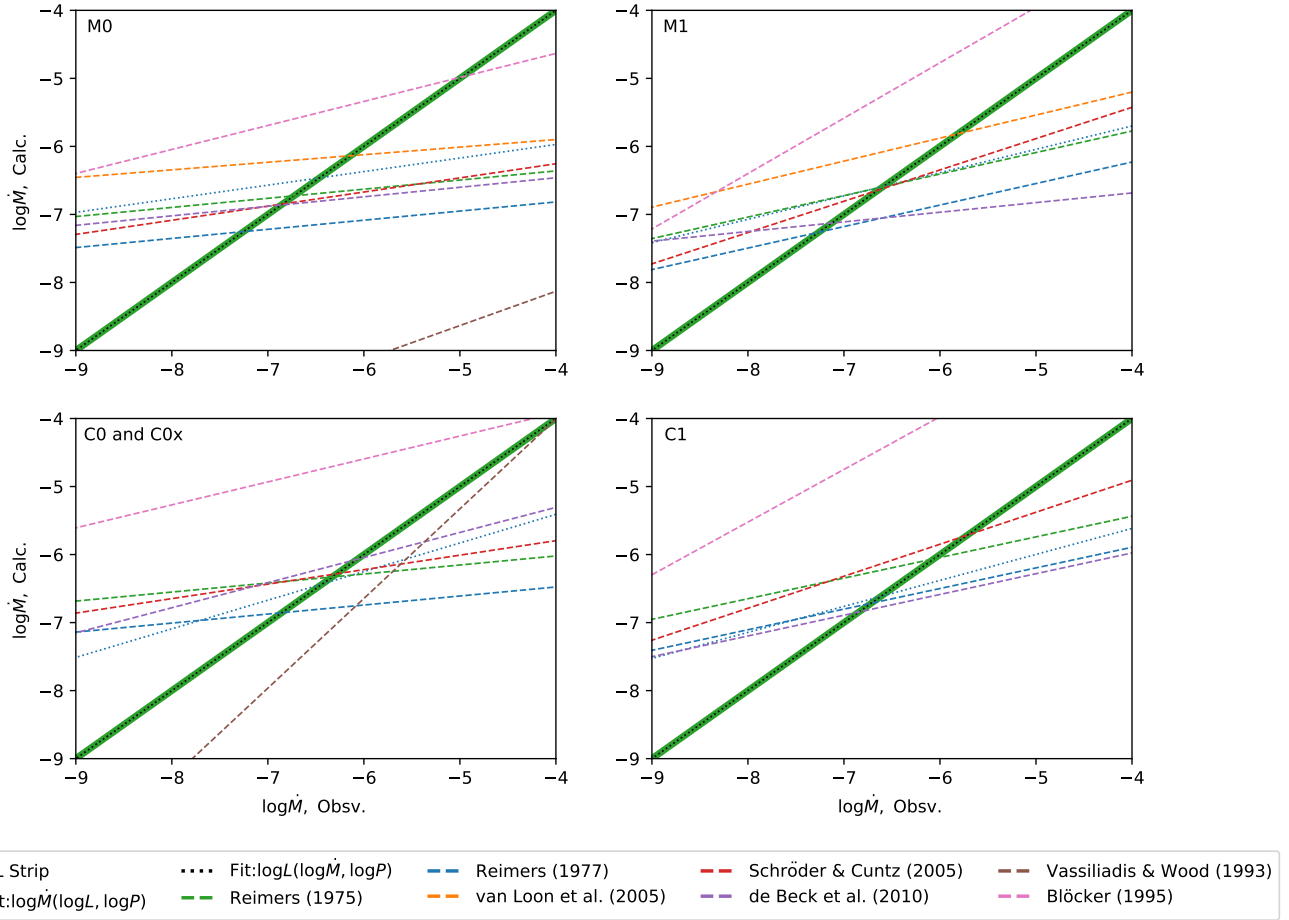


Figure 9. Comparison of the calculated vs. observed mass-loss rates for the formulae we have found and other works. The solid line shows our PL strip fit and matches a 1:1 line by construction (Table 5). The dotted lines show the results of the linear fits (Table 4); the green diagonal line for the PL strip method coincides with what was found by fitting $\log L(\log \dot{M}, \log P)$ (black dotted line). The dashed lines show our fits to equations 22-28. The formulae in those equations have been used to calculate a mass-loss rate (y -axis), and then a line has been fitted to the result of the formula versus the observed mass-loss rate (x -axis). Note that the fit lines have been extended beyond the range of data in order to display the formulae in a single plot and to show their divergent behavior. Nearly all the other relations show the low-slope signature of regression dilution, except the formula from Vassiliadis & Wood (1993). Note that this formula is offset in the M0 panel, due to a difference in mass-loss rate scaling. The spread of data around the various lines can be found in Tables 6 and 7.

7. RESULTS

We can see in Table 7 and Figure 9 that the PL strip provides the overall best fit, with tolerable spread in the predictions and no change in quality over the range of mass-loss rates. These large exponents also tend to agree with the exponential Vassiliadis & Wood (1993) formula, which agrees well with observations of AGB mass loss found in globular clusters by Kamath et al. (2010) and with results from atmospheric modelling (Winters et al. 2000; Bladh et al. 2019a,b). From atmospheric modelling, we also expect larger exponents than those found in the linear fit to \dot{M} , consistent with an abrupt mass-loss phase, but their size is an unresolved question (compare Willson (2000); Höfner & Olofsson (2018)). The PL strip method also has some limits: if the width of the distribution in $\log \dot{M}$ is partly due to observational uncertainty, then correcting for this would make the exponents smaller. If the width of the distribution in $\log L$ is partly due to observational error, then correcting for this would make the exponents bigger.

The observed pattern of stars in $\log P$ or $\log M$ vs. $\log L$ is what we expect if the death-zone analysis holds, given that the sample only contains stars with measurable mass-loss rates between 10^{-8} and 10^{-4} M_{\odot}/yr . This range includes the death line, where $\dot{M} = \dot{M}_{\text{crit}} \equiv M/t_{\text{ev}}$, for any reasonable value of t_{ev} based on evolutionary models. By construction, our power-law exponents produce a strip of the correct width, height, and slope.

The position of the death-line relative to the observations is determined by the value of the coefficient A in the power law (eq. 13) and the value of $t_{\text{ev}} = 1/(d \ln L/dt)$. The coefficient A depends on the dust-to-gas ratio, and is therefore somewhat uncertain. The evolution time is also not trivial to derive, given that many of these stars are experiencing shell flashes. However, if our interpretation of the strip is correct, then by following the evolution of the star in $\log M$ vs. $\log L$ (and thus vs. time), we can position the death-line with respect to the location of the bulk of the stars (see Figure 8).

In Figures 11 and 12, we can see that whether a star becomes a carbon star is primarily determined by stellar mass. Below $1 M_{\odot}$, AGB stars are primarily oxygen-rich; above $1.3 M_{\odot}$ they are primarily carbon-rich. Stars between these masses can be of either type.

8. CONCLUSIONS AND EXTENSION

We have used a sample of 6,889 LMC AGB pulsating and mass-losing stars (Riebel et al. 2012) to derive power-law formulae for mass-loss rates as a function of stellar parameters. By approaching the derivation of a mass-loss formula from the observations in three ways, we have discovered why previous approaches have produced very different formulae: uncertainties in the measurement of L produce regression dilution that reduces the exponents when a fit is made to $\log \dot{M}$ as a function of $\log L$ and $\log P$ (or $\log L$ and other derived stellar parameters). Using this insight, and an analysis of the distribution of the stars in $\log P$ versus $\log L$, we have found formulae that satisfy our expectations that the slope of a fit to $\log \dot{M}_{\text{calc.}}$ versus $\log \dot{M}_{\text{obsv.}}$ should be equal to one. These PL strip formulae also reproduce the distribution in the $\log L$, $\log P$ plane, and show relatively small scatter in the residuals. There is a separate formula for each of four groups, two composition groups ($C/O > 1$ and < 1) and two modes of pulsation, fundamental and first overtone. The exponents in these formulae are closer to what is expected from mass loss models. We conclude that the PL strip method provides the best formulae that can be derived from this set of observations.

The method we have used can be applied to other samples with sufficient numbers of stars at a known distance, such as the Small Magellanic Cloud or Andromeda.

In the process of deriving these formulae we have used published evolutionary models to derive new relations for the period as a function of mass and radius. This allows us to present the formulae in terms of $\log L$ and $\log P$, the most readily observed quantities, or in terms of $\log L$ and $\log M$, appropriate for use with evolutionary models (taking into account that the relations differ according to pulsation mode).

A robust and surprising conclusion of this study is that the death zone is well populated for all four categories of stars — fundamental and overtone pulsators, oxygen- and carbon-rich stars. The carbon and oxygen rich stars separate mostly by mass. The overtone pulsators reach their death zones at slightly higher L than the fundamental mode stars. All four categories are being observed as they go over the cliff.

¹ This work has made use of the NumPy library (Harris et al. 2020), the SciPy Library (Virtanen et al. 2020), IPython software package (Pérez & Granger 2007), the matplotlib library for publication quality graphics (Hunter 2007), and the Scikit-learn library (Pedregosa et al. 2011). Funding for this work has been provided by the New Mexico Space Grant Consortium.

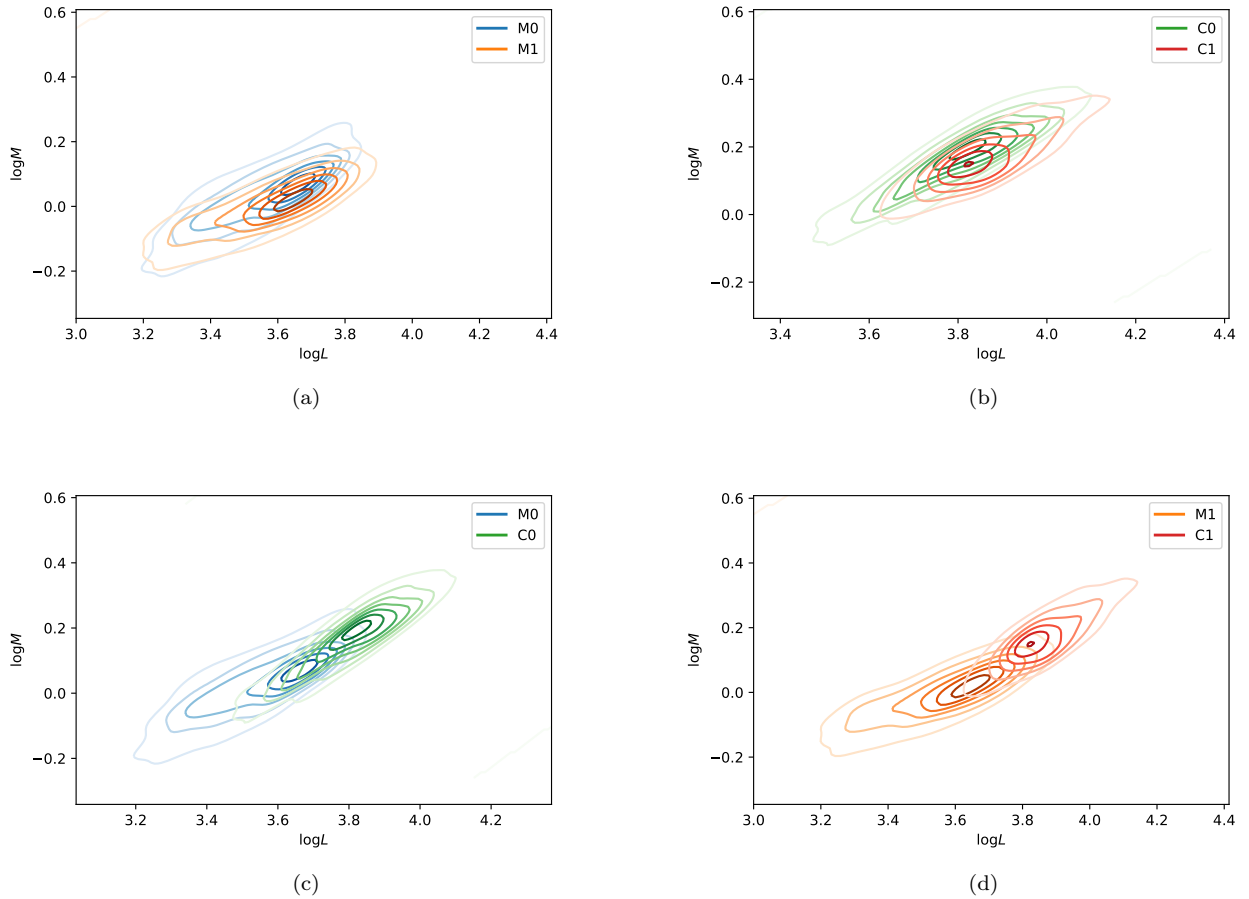


Figure 10. Contour plots depicting the location of the LM strip for the combinations of pulsation mode and C/O composition. The number of stars in each set can be seen in Table 1. The distribution of stars in (c) and (d) is consistent with our assertion that the death zone is well populated for all four categories of stars.

APPENDIX

A. ESTIMATING DUST MASS-LOSS RATE FROM COLOR

While looking for ways to reduce scatter in our $\log \dot{M} \sim \log L + \log P$ fits (see Section 5 for details), we fitted the mass-loss rate to a hyperbolic curve, as in [Busso et al. \(1996\)](#); [Le Bertre & Winters \(1998\)](#); [Matsuura et al. \(2009\)](#); and [Riebel et al. \(2012\)](#). The hyperbolic curves found in these works are of the form

$$\log \dot{M} = \frac{A}{B + (\text{color})} + C, \quad (\text{A1})$$

with the color varying depending on the observational bands available.

Initially, we performed a single-color fit, using $K - [8.0]$ as our primary color as in [Matsuura et al. \(2009\)](#) and [Riebel et al. \(2012\)](#). We found this fit to be unsatisfactory for our purposes for the M0, M1, and C0 stars, so we continued onto a two-color fit, in $K - [8.0]$ and $J - K$.

$$\log \dot{M} = \frac{A}{B + (K - 8.0)} + C - D \times (J - K) \quad (\text{A2})$$

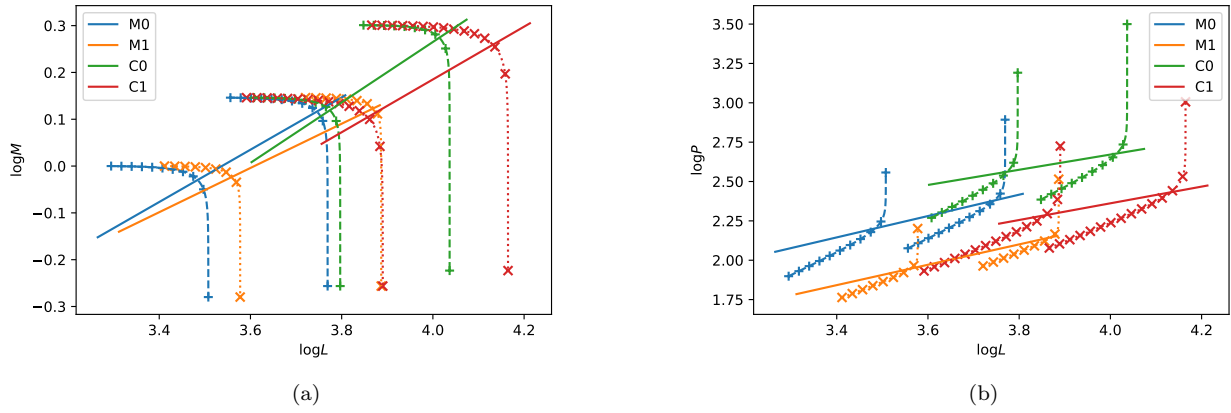


Figure 11. Locations of the death lines for our four sets of stars. The death line is defined by the luminosity and pulsation periods of stars where $\dot{M} = \dot{M}_{\text{crit.}} \equiv M/t_{\text{ev}}$. The luminosity evolution time scale, t_{ev} , is set to 0.6 Myr for the M0 stars, 0.5 Myr for the M1 Stars, and 2.5 Myr for the C0 Stars, and 3.2 Myr for the C1 Stars. Points are marked every $\Delta \log L = 0.015$, with “+” marking fundamental mode points and “x” marking overtone mode points; given $\Delta \log L = 2.3\Delta t/t_{\text{ev}}$, we can see why a majority of stars are expected to be found prior to the death zone. The evolution tracks terminate at a final mass determined using the initial-final mass relation in [Zhao et al. \(2012\)](#). The death lines span the tenth to ninetieth percentile in mass for each data set.

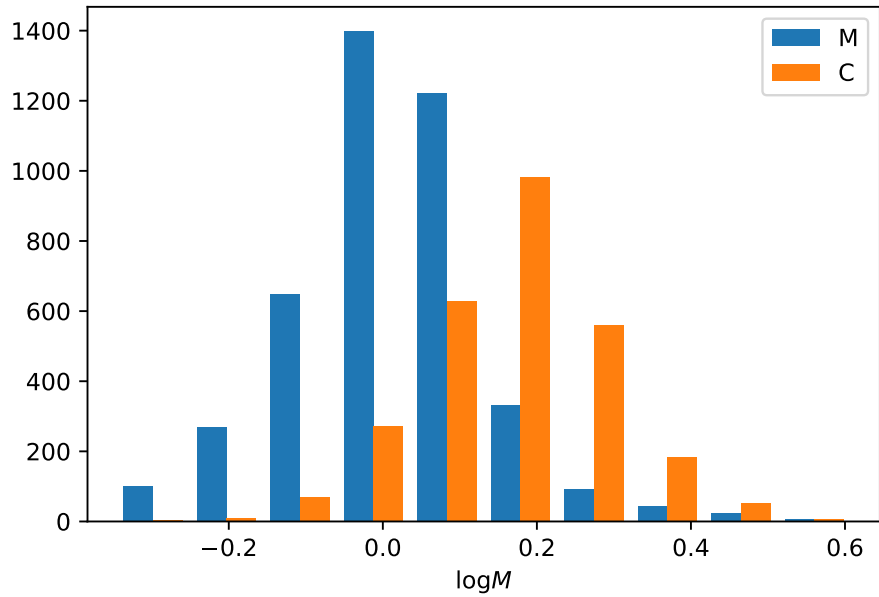


Figure 12. The derived distribution of the masses of the oxygen and carbon-rich stars in our sample, showing that the parameter determining C/O composition is primarily the mass. Mass loss reducing M and shell flashes modulating L introduce scatter in M and may be responsible for most of the overlap in the distributions.

where $J - K$ is treated as a linear correction to the original hyperbolic fit. With this, we were able to obtain fits with significantly better confidences. The results of these fits can be found in [Table 8](#), with graphical depictions in [Figure 13](#).

Examining Figure 13, it is clear that two colors does not completely predict the mass loss of AGB stars. This is unsurprising, as the color is affected directly by factors unique to each star. Despite this, the use of near-infrared J and K bands in addition to a mid- to long-wavelengths (such as [8.0]) allows one to make an estimate of the mass-loss rate of an observed star, without the computational burden of fitting to any models.

Table 8. Fit of $\log \dot{M} = A/((K - [8.0]) + B) + C - D \times (J - K)$

Spectral Class and Pulsation Mode	A	B	C	D
M0	-1.4(1)	0.43(5)	-6.01(8)	0.88(3)
M1	-3.4(5)	0.87(9)	-4.4(2)	1.74(8)
C0	-7(2)	1.9(4)	-5.2(3)	0.34(2)
C0x	-23(9)	5(1)	-2.7(6)	0
C1	-11(2)	2.2(3)	-3.5(3)	0

NOTE—For these fits, a second color was only needed for 3 of the combinations of C/O composition and pulsation mode to be of sufficient quality. If no second color was used, $D = 0$.

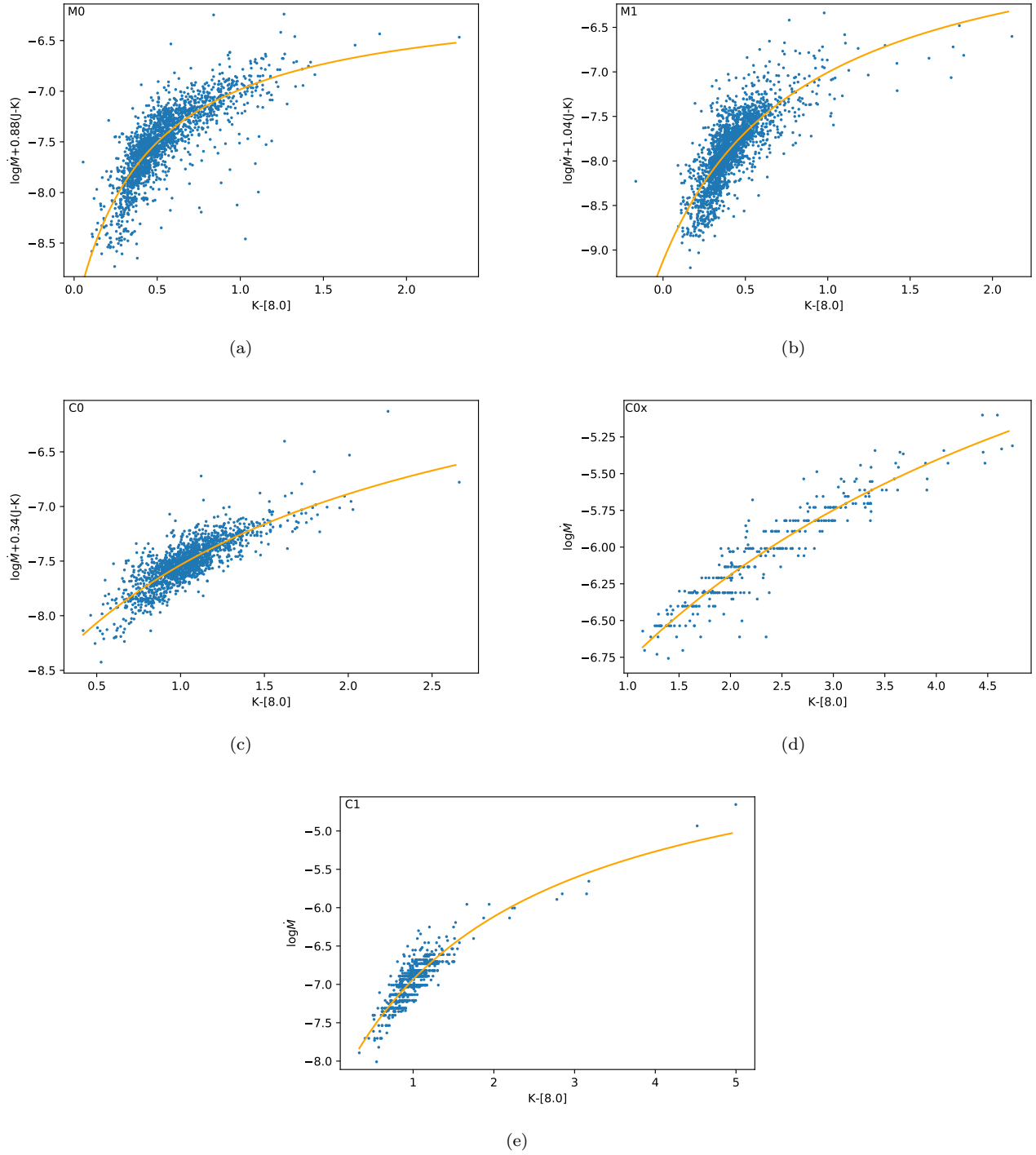


Figure 13. The fit of \dot{M} to the $K - [8.0]$ color, using the function $\log \dot{M} = A/((K - [8.0]) + B) + C - D(J - K)$ is shown. In the case of the oxygen-rich, fundamental-mode pulsators M0, (a); oxygen-rich, first-overtone pulsators M1, (b); and carbon-rich, fundamental-mode pulsators C0, (c), a second color ($J - K$) was used, and is accounted for by including this dependence on the y -axis with $\log \dot{M}$ with the appropriate fitting exponent. For the carbon-rich, extreme, fundamental pulsators C0x, (d) (see Figure 2 for details), and carbon-rich, first-overtone pulsators C1, (e), only a single color was used and thus only $\log \dot{M}$ is found on the y -axis. The values of these fits and their accuracy can be found in Table 8.

REFERENCES

- Alcock, C., Allsman, R. A., Alves, D., et al. 1997, *ApJ*, 486, 697, doi: [10.1086/304535](https://doi.org/10.1086/304535)
- Baud, B., & Habing, H. J. 1983, *A&A*, 127, 73
- Beasor, E. R., & Smith, N. 2022, arXiv e-prints, arXiv:2205.02207. <https://arxiv.org/abs/2205.02207>
- Bladh, S., Eriksson, K., Marigo, P., Liljegren, S., & Aringer, B. 2019a, *A&A*, 623, A119, doi: [10.1051/0004-6361/201834778](https://doi.org/10.1051/0004-6361/201834778)
- Bladh, S., Liljegren, S., Höfner, S., Aringer, B., & Marigo, P. 2019b, *A&A*, 626, A100, doi: [10.1051/0004-6361/201935366](https://doi.org/10.1051/0004-6361/201935366)
- Blöcker, T. 1995, *A&A*, 297, 727
- Blum, R. D., Mould, J. R., Olsen, K. A., et al. 2006, *AJ*, 132, 2034, doi: [10.1086/508227](https://doi.org/10.1086/508227)
- Boothroyd, A. I., & Sackmann, I. J. 1988, *ApJ*, 328, 641, doi: [10.1086/166322](https://doi.org/10.1086/166322)
- Bowen, G. H. 1988, *ApJ*, 329, 299, doi: [10.1086/166378](https://doi.org/10.1086/166378)
- Bowen, G. H., & Willson, L. A. 1991, *ApJL*, 375, L53, doi: [10.1086/186086](https://doi.org/10.1086/186086)
- Boyer, M. L., Srinivasan, S., van Loon, J. T., et al. 2011, *AJ*, 142, 103, doi: [10.1088/0004-6256/142/4/103](https://doi.org/10.1088/0004-6256/142/4/103)
- Bressan, A., Marigo, P., Girardi, L., et al. 2012, *MNRAS*, 427, 127, doi: [10.1111/j.1365-2966.2012.21948.x](https://doi.org/10.1111/j.1365-2966.2012.21948.x)
- Bryan, G. L., Volk, K., & Kwok, S. 1990, *ApJ*, 365, 301, doi: [10.1086/169483](https://doi.org/10.1086/169483)
- Busso, M., Origlia, L., Marengo, M., et al. 1996, *A&A*, 311, 253
- Carroll, R., Ruppert, D., Stefanski, L., & Crainiceanu, C. 2006, *Measurement Error in Nonlinear Models: A Modern Perspective*, Second Edition, Chapman & Hall/CRC Monographs on Statistics & Applied Probability (CRC Press), doi: [10.1201/9781420010138](https://doi.org/10.1201/9781420010138)
- Danilovich, T., Teyssier, D., Justtanont, K., et al. 2015, *A&A*, 581, A60, doi: [10.1051/0004-6361/201526705](https://doi.org/10.1051/0004-6361/201526705)
- De Beck, E., Decin, L., de Koter, A., et al. 2010, *A&A*, 523, A18, doi: [10.1051/0004-6361/200913771](https://doi.org/10.1051/0004-6361/200913771)
- Fazio, G. G., Hora, J. L., Allen, L. E., et al. 2004, *ApJS*, 154, 10, doi: [10.1086/422843](https://doi.org/10.1086/422843)
- Fox, M. W., & Wood, P. R. 1982, *ApJ*, 259, 198, doi: [10.1086/160160](https://doi.org/10.1086/160160)
- Fraser, O. J., Hawley, S. L., & Cook, K. H. 2008, *AJ*, 136, 1242, doi: [10.1088/0004-6256/136/3/1242](https://doi.org/10.1088/0004-6256/136/3/1242)
- Fraser, O. J., Hawley, S. L., Cook, K. H., & Keller, S. C. 2005, *AJ*, 129, 768, doi: [10.1086/426749](https://doi.org/10.1086/426749)
- Frost, C., & Thompson, S. G. 2000, *Journal of the Royal Statistical Society. Series A (Statistics in Society)*, 163, 173. <http://www.jstor.org/stable/2680496>
- Glass, I. S., Schultheis, M., Blommaert, J. A. D. L., et al. 2009, *MNRAS*, 395, L11, doi: [10.1111/j.1745-3933.2009.00628.x](https://doi.org/10.1111/j.1745-3933.2009.00628.x)
- Goldberg, L. 1979, *QJRAS*, 20, 361
- Goldman, S. R., van Loon, J. T., Zijlstra, A. A., et al. 2017, *MNRAS*, 465, 403, doi: [10.1093/mnras/stw2708](https://doi.org/10.1093/mnras/stw2708)
- Groenewegen, M. A. T., & Sloan, G. C. 2018, *A&A*, 609, A114, doi: [10.1051/0004-6361/201731089](https://doi.org/10.1051/0004-6361/201731089)
- Guandalini, R., Busso, M., Ciprini, S., Silvestro, G., & Persi, P. 2006, *A&A*, 445, 1069, doi: [10.1051/0004-6361:20053208](https://doi.org/10.1051/0004-6361:20053208)
- Gullieuszik, M., Groenewegen, M. A. T., Cioni, M. R. L., et al. 2012, *A&A*, 537, A105, doi: [10.1051/0004-6361/201117493](https://doi.org/10.1051/0004-6361/201117493)
- Harris, C. R., Millman, K. J., van der Walt, S. J., et al. 2020, *Nature*, 585, 357, doi: [10.1038/s41586-020-2649-2](https://doi.org/10.1038/s41586-020-2649-2)
- Harris, J., & Zaritsky, D. 2009, *AJ*, 138, 1243, doi: [10.1088/0004-6256/138/5/1243](https://doi.org/10.1088/0004-6256/138/5/1243)
- Herwig, F. 2005, *ARA&A*, 43, 435, doi: [10.1146/annurev.astro.43.072103.150600](https://doi.org/10.1146/annurev.astro.43.072103.150600)
- Höfner, S., Bladh, S., Aringer, B., & Ahuja, R. 2016, *A&A*, 594, A108, doi: [10.1051/0004-6361/201628424](https://doi.org/10.1051/0004-6361/201628424)
- Höfner, S., Bladh, S., Aringer, B., & Eriksson, K. 2022, *A&A*, 657, A109, doi: [10.1051/0004-6361/202141224](https://doi.org/10.1051/0004-6361/202141224)
- Höfner, S., Gautschy-Loidl, R., Aringer, B., & Jørgensen, U. G. 2003, *A&A*, 399, 589, doi: [10.1051/0004-6361:20021757](https://doi.org/10.1051/0004-6361:20021757)
- Höfner, S., & Olofsson, H. 2018, *A&A Rv*, 26, 1, doi: [10.1007/s00159-017-0106-5](https://doi.org/10.1007/s00159-017-0106-5)
- Hunter, J. D. 2007, *Computing In Science & Engineering*, 9, 90
- Iben, Jr., I. 1984, *ApJ*, 277, 333, doi: [10.1086/161700](https://doi.org/10.1086/161700)
- Ita, Y., Tanabé, T., Matsunaga, N., et al. 2004, *MNRAS*, 347, 720, doi: [10.1111/j.1365-2966.2004.07257.x](https://doi.org/10.1111/j.1365-2966.2004.07257.x)
- Kalirai, J. S., Marigo, P., & Tremblay, P.-E. 2014, *ApJ*, 782, 17, doi: [10.1088/0004-637X/782/1/17](https://doi.org/10.1088/0004-637X/782/1/17)
- Kamath, D., Wood, P. R., Soszyński, I., & Lebzelter, T. 2010, *MNRAS*, 408, 522, doi: [10.1111/j.1365-2966.2010.17137.x](https://doi.org/10.1111/j.1365-2966.2010.17137.x)
- Kippenhahn, R., Weigert, A., & Weiss, A. 2013, *Stellar Structure and Evolution* (Springer Science+Business Media), doi: [10.1007/978-3-642-30304-3](https://doi.org/10.1007/978-3-642-30304-3)
- Kudritzki, R. P., & Reimers, D. 1978, *A&A*, 70, 227
- Le Bertre, T., & Winters, J. M. 1998, *A&A*, 334, 173
- Marigo, P., Bressan, A., Nanni, A., Girardi, L., & Pumo, M. L. 2013, *MNRAS*, 434, 488, doi: [10.1093/mnras/stt1034](https://doi.org/10.1093/mnras/stt1034)
- Matsuura, M., Barlow, M. J., Zijlstra, A. A., et al. 2009, *MNRAS*, 396, 918, doi: [10.1111/j.1365-2966.2009.14743.x](https://doi.org/10.1111/j.1365-2966.2009.14743.x)

- McDonald, I., De Beck, E., Zijlstra, A. A., & Lagadec, E. 2018, *MNRAS*, 481, 4984, doi: [10.1093/mnras/sty2607](https://doi.org/10.1093/mnras/sty2607)
- Meixner, M., Gordon, K. D., Indebetouw, R., et al. 2006, *AJ*, 132, 2268, doi: [10.1086/508185](https://doi.org/10.1086/508185)
- Ostlie, D. A., & Cox, A. N. 1986, *ApJ*, 311, 864, doi: [10.1086/164824](https://doi.org/10.1086/164824)
- Pastorelli, G., Marigo, P., Girardi, L., et al. 2020, *MNRAS*, 498, 3283, doi: [10.1093/mnras/staa2565](https://doi.org/10.1093/mnras/staa2565)
- Pedregosa, F., Varoquaux, G., Gramfort, A., et al. 2011, *Journal of Machine Learning Research*, 12, 2825
- Pérez, F., & Granger, B. E. 2007, *Computing in Science and Engineering*, 9, 21, doi: [10.1109/MCSE.2007.53](https://doi.org/10.1109/MCSE.2007.53)
- Reimers, D. 1975, *Circumstellar envelopes and mass loss of red giant stars* (Springer-Verlag New York, Inc.), 229–256
- . 1977, *A&A*, 61, 217
- Riebel, D., Meixner, M., Fraser, O., et al. 2010, *ApJ*, 723, 1195, doi: [10.1088/0004-637X/723/2/1195](https://doi.org/10.1088/0004-637X/723/2/1195)
- Riebel, D., Srinivasan, S., Sargent, B., & Meixner, M. 2012, *ApJ*, 753, 71, doi: [10.1088/0004-637X/753/1/71](https://doi.org/10.1088/0004-637X/753/1/71)
- Sargent, B. A., Srinivasan, S., & Meixner, M. 2011, *ApJ*, 728, 93, doi: [10.1088/0004-637X/728/2/93](https://doi.org/10.1088/0004-637X/728/2/93)
- Schröder, K.-P., & Cuntz, M. 2005, *ApJL*, 630, L73, doi: [10.1086/491579](https://doi.org/10.1086/491579)
- Seabold, S., & Perktold, J. 2010, in *9th Python in Science Conference*
- Skrutskie, M. F., Cutri, R. M., Stiening, R., et al. 2006, *AJ*, 131, 1163, doi: [10.1086/498708](https://doi.org/10.1086/498708)
- Spearman, C. 1904, *The American Journal of Psychology*, 15, 72. <http://www.jstor.org/stable/1412159>
- Spitzer, L. 1978, *Physical processes in the interstellar medium* (John Wiley & Sons Inc), doi: [10.1002/9783527617722](https://doi.org/10.1002/9783527617722)
- Srinivasan, S., Sargent, B. A., & Meixner, M. 2011, *A&A*, 532, A54, doi: [10.1051/0004-6361/201117033](https://doi.org/10.1051/0004-6361/201117033)
- Srinivasan, S., Meixner, M., Leitherer, C., et al. 2009, *AJ*, 137, 4810, doi: [10.1088/0004-6256/137/6/4810](https://doi.org/10.1088/0004-6256/137/6/4810)
- Tang, J., Bressan, A., Rosenfield, P., et al. 2014, *MNRAS*, 445, 4287, doi: [10.1093/mnras/stu2029](https://doi.org/10.1093/mnras/stu2029)
- Trabucchi, M., Wood, P. R., Montalbán, J., et al. 2019, *MNRAS*, 482, 929, doi: [10.1093/mnras/sty2745](https://doi.org/10.1093/mnras/sty2745)
- Trabucchi, M., Wood, P. R., Mowlavi, N., et al. 2021, *MNRAS*, 500, 1575, doi: [10.1093/mnras/staa3356](https://doi.org/10.1093/mnras/staa3356)
- van Loon, J. T. 2000, *A&A*, 354, 125. <https://arxiv.org/abs/astro-ph/9912053>
- van Loon, J. T., Cioni, M. R. L., Zijlstra, A. A., & Loup, C. 2005, *A&A*, 438, 273, doi: [10.1051/0004-6361:20042555](https://doi.org/10.1051/0004-6361:20042555)
- van Loon, J. T., Cohen, M., Oliveira, J. M., et al. 2008, *A&A*, 487, 1055, doi: [10.1051/0004-6361:200810036](https://doi.org/10.1051/0004-6361:200810036)
- Vassiliadis, E., & Wood, P. R. 1993, *ApJ*, 413, 641, doi: [10.1086/173033](https://doi.org/10.1086/173033)
- Virtanen, P., Gommers, R., Oliphant, T. E., et al. 2020, *Nature Methods*, 17, 261, doi: <https://doi.org/10.1038/s41592-019-0686-2>
- Volk, K., & Kwok, S. 1988, *ApJ*, 331, 435, doi: [10.1086/166570](https://doi.org/10.1086/166570)
- Wachter, A., Schröder, K. P., Winters, J. M., Arndt, T. U., & Sedlmayr, E. 2002, *A&A*, 384, 452, doi: [10.1051/0004-6361:20020022](https://doi.org/10.1051/0004-6361:20020022)
- Wang, Q., Willson, L. A., & Kawaler, S. D. 2009, in *Astronomical Society of the Pacific Conference Series*, Vol. 412, *The Biggest, Baddest, Coolest Stars*, ed. D. G. Luttermoser, B. J. Smith, & R. E. Stencel, 255
- Willson, L. A. 2000, *ARA&A*, 38, 573, doi: [10.1146/annurev.astro.38.1.573](https://doi.org/10.1146/annurev.astro.38.1.573)
- Willson, L. A., Struck, C., Wang, Q., & Kawaler, S. D. 2008, *Physica Scripta Volume T*, 133, 014008, doi: [10.1088/0031-8949/2008/T133/014008](https://doi.org/10.1088/0031-8949/2008/T133/014008)
- Winters, J. M., Le Bertre, T., Jeong, K. S., Helling, C., & Sedlmayr, E. 2000, *A&A*, 361, 641
- Wood, P. R., Alcock, C., Allsman, R. A., et al. 1999, in *IAU Symposium*, Vol. 191, *Asymptotic Giant Branch Stars*, ed. T. Le Bertre, A. Lebre, & C. Waelkens, 151
- Zaritsky, D., Harris, J., Thompson, I. B., & Grebel, E. K. 2004, *AJ*, 128, 1606, doi: [10.1086/423910](https://doi.org/10.1086/423910)
- Zhao, J. K., Oswalt, T. D., Willson, L. A., Wang, Q., & Zhao, G. 2012, *ApJ*, 746, 144, doi: [10.1088/0004-637X/746/2/144](https://doi.org/10.1088/0004-637X/746/2/144)